Structure and petrology of newly discovered volcanic centers in the northern Kermadec–southern Tofua arc, South Pacific Ocean

Ian J. Graham,[1] Agnes G. Reyes,[1] Ian C. Wright,[2] Kimberley M. Peckett,[3] Ian E. M. Smith,[3] and Richard J. Arculus[4]

Received 18 October 2007; revised 18 June 2008; accepted 10 July 2008; published 30 August 2008.

[1] The NZAPLUME III expedition of September–October 2004 to the northern Kermadec–southern Tofua (NKST) arc, between 28°52′S and 25°07′S, resulted in the discovery of at least seven new submarine volcanic centers and a substantial caldera complex adjacent to the previously known Monowai Seamount. The volcanic centers form a sublinear chain that coincides with the Kermadec Ridge crest in the south (Hinetapeka) and diverges ~45 km westward of the ridge crest in the north ("V") just to the south of where the Louisville Ridge intersects with the arc. All of the centers contain calderas or caldera-like structures, as well as multiple cones, domes, fissure ridges, and vent fields. All show signs of recent eruptive and current hydrothermal activity. There are strong structural controls on edifice location, with cones and fissure ridges typically associated with faulting parallel to the regional ~12° strike of the arc front. Several of the calderas are ellipsoidal, orientated northwest–southeast in the general direction of least compressive stress. Sampled volcanic rocks, representing the most recently erupted lavas, are all low-K tholeiites. Two of the centers, Gamble and Rakahore, yielded only high-silica dacite to rhyolite (69–74 wt% silica), whereas two others, Monowai and "V," yielded only basalt to andesite (48–63 wt% silica). Mineral assemblages are plagioclase-pyroxene dominated, with accessory Fe-Ti oxides, apatite, olivine, and quartz/tridymite/cristobalite, typical of dry volcanic arc systems. Hornblende occurs only in a felsitic rhyolite from Hinepuia volcanic center, and zircon is absent. Glass contents range to 57% in basalts–andesites (mean 20%), and 97% in andesites–rhyolites (mean 59%) and other quench textures, including swallow-tailed, plumose, or dendritic crystal forms and crystallites, are common. Most lavas are highly vesicular (≤63%; mean 28%) and have low volatile contents (mostly <2 wt%) which, together with the occurrence of tridymite or cristobalite, indicates explosive eruption and rapid cooling. Exceptions are rocks from "U" volcanic center, which have low vesicularity and low glass contents across a wide compositional range, indicating effusive eruption. Disequilibrium mineral textures, the frequent occurrence of xenoliths and xenocrysts, and macroscopic evidence for magma mingling indicate that many of the lavas are hybrids, having resided only a short time in upper crustal reservoirs prior to eruption. Silicic magmas are major components of NKST arc volcanism and caldera formation is the dominant eruptive style. The scale of silicic magmatism is in marked contrast to the dominant basaltic–andesitic magmatism in the southern Kermadec arc. With evidence from other arcs, silicic magmatism is now recognized as a major feature of intraoceanic arcs globally.

Citation: Graham, I. J., A. G. Reyes, I. C. Wright, K. M. Peckett, I. E. M. Smith, and R. J. Arculus (2008), Structure and petrology of newly discovered volcanic centers in the northern Kermadec–southern Tofua arc, South Pacific Ocean, *J. Geophys. Res.*, *113*, B08S02, doi:10.1029/2007JB005453.

1. Introduction

[2] The 2500 km-long Kermadec–Tofua arc (Figure 1a) is an intraoceanic subduction system with relatively simple but fast plate convergence. Prior to the mid-1990s only the Tongan and Kermadec islands and the Monowai and Rumble/Silent seamounts were known. Since then the entire arc has been systematically multibeam mapped, revealing numerous further submarine volcanic centers spaced 30–50 km apart [*Wright and Gamble*, 1999; *de Ronde et al.*, 2001; *Wright et*

[1]GNS Science, Lower Hutt, New Zealand.
[2]National Institute of Water and Atmospheric Research, Wellington, New Zealand.
[3]School of Geography, Geology and Environmental Science, University of Auckland, Auckland, New Zealand.
[4]Department of Geology, Australian National University, Canberra, ACT, Australia.

0148-0227/08/2007JB005453$09.00

al., 2006; *de Ronde et al.*, 2006; *Smith and Price*, 2006]. Along the Kermadec–southern Tofua arc to 25°S, a total of 37 volcanic centers have been identified, most of which have been sampled for lavas, minerals, or vent fluids.

[3] In this paper we present the first volcanological and petrological analysis of the northern Kermadec–southern Tofua (NKST) arc front (Figure 1b), from 28°52′S to 25°07′S as surveyed the NZAPLUME III expedition in September–October 2004. During this expedition, several new volcanic centers, as well as a large caldera complex near Monowai Seamount, were discovered and mapped.

2. Regional Setting

[4] The Kermadec–Tofua subduction system (Figure 1a) involves mainly convergence of the Pacific and Australian plates, with the Niuaf'ou, Tonga, and Kermadec microplates accommodating back-arc spreading and rifting in the Lau Basin and Havre Trough [*Ruellan et al.*, 2003]. Plate motion is relatively fast, increasing from ~49 mm a^{-1} at 36°S to ~69 mm a^{-1} at 25°S. From ~37°S to 32°S, the Kermadec Ridge is relatively narrow with the active arc front located to the west of it [*Wright*, 1997] and the Havre Trough is a deep and structurally complex region of backarc rifting [*Wright et al.*, 1996]. From ~32°S to 28°30′S, the ridge is wider, the arc front is on or near the ridge crest, and the Havre Trough is shallower and more thickly sedimented [*Delteil et al.*, 2002]. Steepening of the subducting slab [*Reyners*, 1989] results in a decrease of the arc front trench distance from ~300 km at 37°S to ~185 km at 32°S, north of which a nearly constant separation is maintained.

[5] The Kermadec–Tofua subduction system between ~38°S and 25°S is divided into several sectors (Figures 1a and 1b) reflecting longitudinal changes in structure. The TVZ sector extends from onshore New Zealand to 36°40′S, where the Vening Meinez Fracture Zone marks the transition from continental arc to intraoceanic arc [*Wright*, 1994]. From there the SKA sector extends to 34°10′S, where the northern limit of the Raukumara fore-arc basin coincides with subduction of the ~17 km thick oceanic Hikurangi Plateau beneath the arc. Northward within the SKA sector, the Kermadec Ridge gradually emerges from beneath sediments of the Raukumara Basin at 2400 mbsl. SKA volcanic centers are all located 20–30 km to the west of the ridge at water depths of 2500–3000 mbsl. Most consist of basaltic to andesitic stratovolcanoes with parasitic or satellite cones, but three are dominated by calderas two of which (Healy and Brothers) are known to be dacitic [*Wright and Gamble*, 1999; *Wright et al.*, 2003; *de Ronde et al.*, 2003]. Evidence of recent volcanic activity occurs in the east of several paired volcanic centers [*Wright et al.*, 1996], and active hydrothermal venting [*de Ronde et al.*, 2001; *Baker et al.*, 2003], sometimes associated with massive sulfide mineralization [*Wright et al.*, 1998; *de Ronde et al.*, 2003, 2005], occurs at 50% of the centers.

[6] The MKA sector extends to 28°30′S, and may be subdivided into northern (N-MKA) and southern (S-MKA) segments at 32°S, where the arc front merges with the ridge. The S-MKA sector contains the deepest volcanic centers along the Kermadec arc and those most distant from the Kermadec Ridge [*Wright et al.*, 2006]. All are dominated by stratovolcanoes. The centers are similar lithologically to those within the SKA sector but are more widely spaced (~45 km versus 30 km). Within the N-MKA sector, volcanic centers are located on, or close to, the crest of the Kermadec Ridge, and include both calderas and stratovolcanoes. This sector contains the Kermadec Islands, the emergent summits of large stratovolcanoes formed by coalesced strombolian and phreatomagmatic deposits. Raoul and Macauley islands largely comprise basalt–andesite, but dacitic pumice is also widespread. Recent episodes of voluminous silicic volcanism were associated with caldera formation, pyroclastic flows and plinian eruptions [*Lloyd et al.*, 1996; *Worthington et al.*, 1999; *Smith et al.*, 2003a]. The northernmost volcanic center within the N-MKA sector is Hinetapeka, the largest and most complex of those discovered during NZAPLUME III (Table 1). North of Hinetapeka, and possibly contiguous with it, is "OP," an inactive volcanic center.

[7] The NKA sector extends northward between "OP" to 26°S, where the ridge is slightly deeper (Figure 1b). Volcanic centers within this sector (Putoto to Hinepuia) are more widely and evenly spaced (mean 52 km; Table 1), and are dominated by calderas or caldera-like edifices. The southernmost STA volcanic centers, Monowai, "U" and "V" have formed on the broader and shallower part of the ridge, just to the south of where the Louisville Ridge and the Tonga Ridge intersect (Figure 1a).

3. Data Acquisition

[8] Seafloor mapping was undertaken using R/V *Tangaroa*'s EM300 multibeam system. Details of positional accuracies and gridding procedures are given by *Wright et al.* [2006]. Rock sampling was undertaken on all the newly discovered volcanic centers except "OP." Dredging targeted major edifices within each volcanic center with the aim of obtaining a full range of lithologies. However, the summits of scoria cones, domes, and stratovolcanoes proved easier to sample, often yielding full dredge loads after less than 10 min towing (Table 2). The calderas, particularly the caldera floors, required longer tows for significantly lower yields. Hence, the dredging operation applied a difficult-to-avoid bias to the sampling. As well, some parts of the more complex volcanic centers were not sampled. Selection procedures, on-deck and onshore, of representative samples for further study were designed to ensure no further bias. Weightings based on shipboard observations and constructional volume calculations (Appendix A) provide empirical estimates of compositional ranges and relative proportions of different lithologies recovered from individual volcanic centers. The dredging bias, however, means that these estimates relate mainly to the composition of relatively recent eruptives and are not indicative of the volcanic centers as a whole.

[9] In preparation for analysis, the inner, fresh sections of samples were crushed to centimeter-sized chips and washed in distilled water for several hours (lava) or days (scoria and pumice). Washed chips were dried at 60°C and hand picked for the freshest material for thin section making and for powdering in agate for chemical analysis. Detailed petrological analysis and evaluation [*Reyes*, 2008] using transmitted light microscopy was undertaken on 85 selected samples (260–2700 point counts on each sample; ~1000 counts on average).

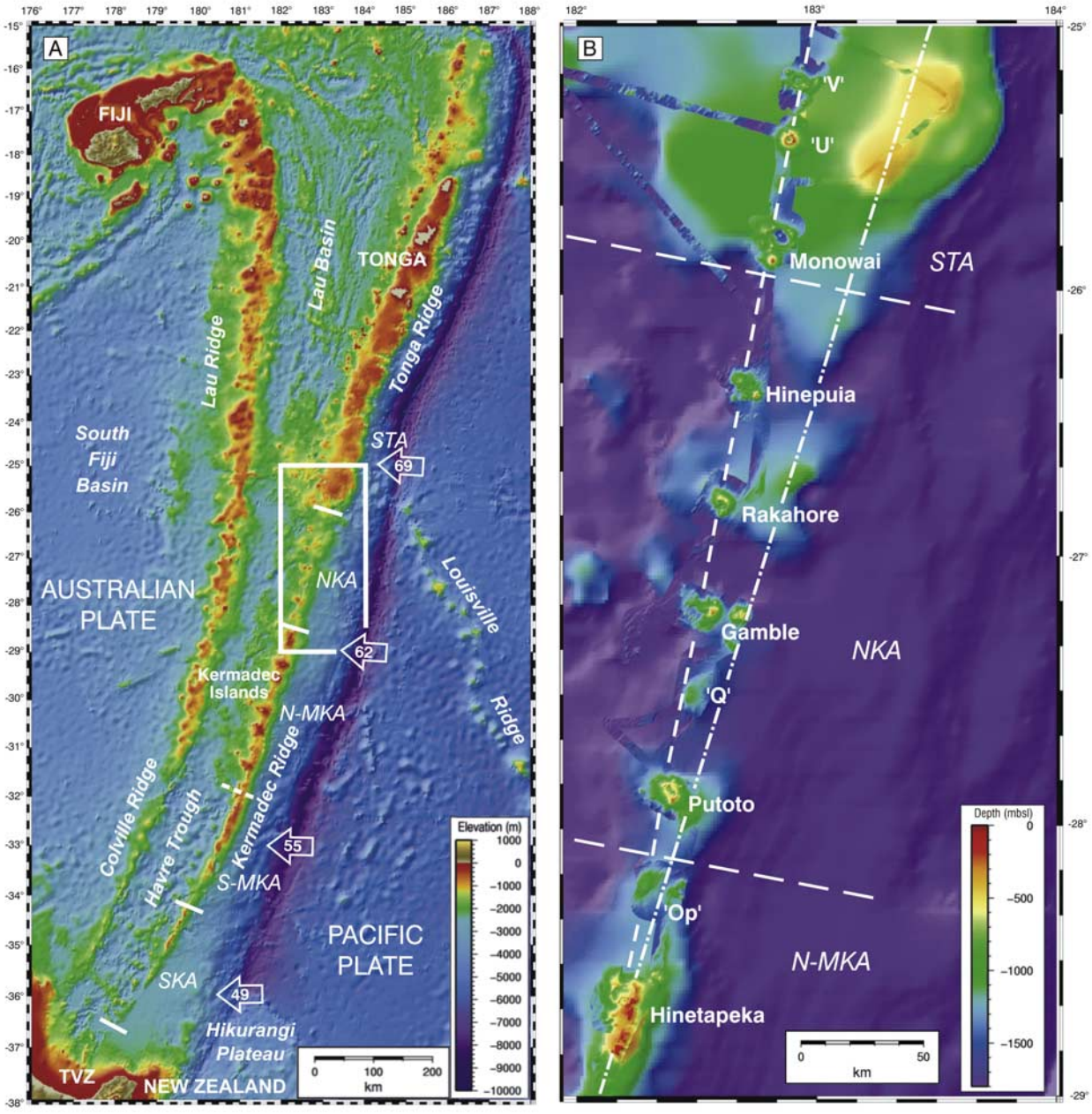

Figure 1. (a) Regional tectonic setting of the Kermadec–Tofua and Colville–Lau arc systems. Relative Pacific–Australian plate motions (mm a^{-1}), shown by arrows, are after *DeMets et al.* [1994]. The Kermadec and Tofua arc-front sectors represent minor modifications of previous interpretations [*de Ronde et al.*, 2006; *Smith and Price*, 2006; *Wright et al.*, 2006] and are (south to north): Taupo Volcanic Zone (TVZ); southern Kermadec arc (SKA); middle Kermadec arc (MKA; S = southern part; N = northern part); northern Kermadec arc (NKA); southern Tofua arc (STA). (b) Enlargement of the central Kermadec–Tofua arc (rectangular area in Figure 1a), with multibeam maps of individual volcanic centers superimposed on large-scale satellite bathymetry. Here "mbsl" is meters below sea level.

[10] XRF major element analysis was undertaken at the University of Auckland. All samples with high loss on ignition (LOI) and/or more than 5% xenoliths plus secondary alteration (including seafloor sedimentary material) are excluded from the present discussion; the nature and significance of such contamination will be reported separately. Analyses used in calculating mean compositions were weighted according to the number of similar compositions recorded (Appendix A), and the relative volumes of the sampled edifices. Constructional volumes (Table 1) of cones and domes were calculated from gridded bathymetry data above curved basal surfaces using GIS terrain models. For calderas, "destructional" volumes relating to the fill void from floor to rim were also calculated (Table 3), but not

Table 1. NKST Volcanic Center Statistics

Volcanic Center[a]	Location[b]	Spacing[c] (km)	Dimensions[d] (km)	Area[e] (km^2)	Volume[f] (km^3)	Summit[g] (mbsl)	Relief[h] (m)
Hinetapeka ("O")	28.59°S 177.82°W	76	34.8 × 16.0	437	166	96	957
"OP"[i]	28.23°S 177.65°W	42	22 × 11	252	43	994	406
Putoto ("P")	27.68°S 177.61°W	61	19.6 × 13.8	212	61	225	1275
Gamble ("R")	27.20°S 177.41°W	57	24.0 × 16.0	302	47	226	1281
Rakahore ("S")	26 .81°S 177.40°W	43	13.8 × 11.3	123	29	560	1145
Hinepuia ("T")	26.39°S 177.26°W	49	17.5 × 11.5	158	28	298	1107
Monowai	25.95°S 177.18°W	48	23.9 × 22.0	412	42	131	1469
"U"	25.44°S 177.11°W	59	15.2 × 14.2	170	29	142	945
"V"	25.19°S 177.06°W	28	13.1 × 12.2	126	18	476	924

[a]Original field labels are given in brackets (see *de Ronde et al.*, 2006).
[b]Approximate midpoint.
[c]Distance to the center immediately to the south (for Hinetapeka, this is Raoul).
[d]Intersection of cross-section lines with center boundaries (see Figures 2 and 5–7).
[e]On the basis of the given dimensions, assuming an elliptical shape.
[f]Constructional volumes, the sum of volume calculations for all major edifices within each volcanic center (excluding calderas).
[g]Shallowest point (meters below sea level).
[h]Difference between the summit depth and the baseline depth immediately below it.
[i]Size estimates for OP are highly uncertain due to incomplete mapping.

included in the volcanic center totals since the true fate of the ejected material is unknown.

[11] To avoid a plethora of names for individual volcanic edifices and calderas and to allow systematic comparisons of volcanic spacings and eruptive volumes, assemblages of closely related volcanic edifices are referred to here as "volcanic centers," following the usage of *de Ronde et al.* [2006]. Within or close to the volcanic centers, individual edifices are named systematically using nomenclature based on an acronym of the volcanic center name. For example, with respect to Hinetapeka volcanic center (Figure 2), HtC1–HtC7 refer to calderas (numbered from oldest to youngest); HtR1 and HtR2 refer to inferred resurgent cones within the calderas; HtP1–HtP7 refer to parasitic cones on the rims of calderas or the slopes of stratovolcanoes (numbered clockwise from north center); and HtS1–HtS3 refer to satellite cones outside the volcanic center. A dominating stratovolcano or dome complex within a volcanic center may be designated "V" (for example Monowai volcano, MoV).

[12] The outer limits of the volcanic centers are imprecise and often arbitrary. Volcanic terrain complexity (i.e., the distribution of vent fields, fissure ridges, dikes, and sector collapse structures), incomplete multibeam mapping, and buttressing of the volcanic centers against the Kermadec Ridge, mean that the given dimensions and volumes are minima. Cones, vent fields and fissure ridges outside the volcanic center limits are deemed to be satellite to the main volcanism, although some may be genetically linked to features within the center.

[13] Following *Lipman* [1997], *Wright and Gamble* [1999], and others, "caldera" is used here for interpreted syn-eruptive collapse overlying a discharging magma chamber, without reference to size or magma composition, and "crater" is used where volcanic ejecta form constructional collars surrounding a vent. This distinction can be subtle when based purely on seafloor morphology, particularly where the structure is overprinted or dismembered. Generally, however, flat-floored structures are interpreted to be calderas and inverted cones or paraboloid structures are interpreted to be craters. Most small constructional edifices are interpreted to be scoria cones, particularly if they have a discernable crater, but cone-shaped edifices in the floors of calderas may be better described as resurgent domes, particularly where their compositions are similar to caldera rims and walls.

4. N-MKA Volcanic Centers

4.1. Hinetapeka

[14] Hinetapeka (Figure 2) is a complex volcanic center near the crest of the Kermadec Ridge, the largest of the

Table 2. NZAPLUME III Dredging Bias

Edifice Type	Average Run Time (min)	Average Yield[a] (%)	Number of Runs
Large cone (summit)	11	85	13
Large cone (flank)	14	52	7
Small cone (summit and flank)	11	51	12
Caldera rim	18	50	9
Caldera wall	19	48	5
Caldera floor	35	25	3

[a]Estimated visually, including unsuccessful runs.

Table 3. Caldera Characteristics

Edifice	Dimensions[a] (km)	Area[b] (km^2)	Volume[c] (km^3)	Ellipticity[d] (°)	Floor Depth[e] (mbsl)	Rim Depth[e] (mbsl)
HtC1[f]	14 × 10	110	6.0	unknown	500	250
HtC2	8.5 × 8.3	55.8	3.0	none	750	350
HtC3	4.9 × 3.1	11.9	0.3	085	610	250
HtC4	1.9 × 1.2	1.8	0.02	125	560	250
HtC5	1.2 × 1.2	1.2	0.02	none	360	200
HtC6	1.7 × 1.7	2.4	0.03	none	260	150
HtC7	1.3 × 1.0	1.1	0.05	030	260	165
OPC1[f]	3 × 3	30	0.2	unknown	1350	1000
PuC1	3.5 × 2.7	7.2	0.4	110	770	585
PuC2	3.4 × 2.9	7.7	0.6	130	770	585
GaC1	11.4 × 7.1	95.4	1.9	090	1400	1150
GaC2	8.1 × 4.7	50.4	0.9	125	1385	1060
RkC1	5.0 × 4.7	18.3	1.9	none	1000	580
RkC2	3.0 × 2.9	6.8	0.5	none	1200	650
HpC1	6.8 × 4.9	26.2	0.9	090	1120	n.d.
HpC2	3.7 × 3.2	9.2	0.25	none	1045	800
MoC1	11.8 × 9.1	84.0	14.6	120	1125	800
MoC2	7.9 × 5.7	35.3	5.6	150	1590	1000
UC1	3.8 × 3.8	11.2	1.4	none	835	170
VC1	8.8 × 6.5	44.9	3.1	120	1155	900
VC2	6.4 × 5.0	25.1	3.1	120	1155	680

[a]Longest and shortest axes.
[b]On the basis of the given dimensions, assuming an elliptical shape.
[c]"Destructional" volume based on the area and average relief.
[d]Orientation of long axis.
[e]Average depth (meters below sea level).
[f]High uncertainty due to incomplete mapping, or rims obscured by faulting, sector collapse, etc.

NKST centers in both area and constructional volume (Table 1). It has an elongated, irregular shape, orientated in line with the regional trend of the other NKST centers (Figure 1b). In the northwest are seven nested calderas (HtC1–HtC7) ranging in size from 0.02 to 6 km^3 (Table 3), which are buttressed against a flat-topped, highstanding volcanic edifice (HtP2, HtP3) forming the eastern margin. Relative relief decreases by several hundred meters east–west across the center (Figure 2a cross sections), accentuated by major sector collapses. Faults are rare, except on the outer flanks, where they have a dominant NNE strike.

[15] The relative ages of the seven calderas are determined on the basis of their morphology and nesting pattern (Figure 2a inset). The rim of HtC1 is poorly defined due to sector collapse and burial but appears to enclose all the other calderas, which become progressively younger eastward across the center. On the northwestern rim of HtC1, the dissected cone HtP7 is probably coeval with HtC1 and is truncated by HtC2. The prominent northern sector collapse has well-defined margins and undulating topography and may have collapsed during formation of HtC2. The collapse feature southwest from HtP6, shown by multibeam backscatter imagery to contain mainly talus and older lava flows, probably occurred during formation of HtC3. HtR2 is a likely resurgent dome within HtC3 that lies on a ~8 km long fissure ridge associated with southwest dipping faults extending from HtC6 northwestward across the caldera floor. Plume surveying [*de Ronde et al.*, 2006] indicates relatively strong hydrothermal venting from the summit of HtR2 and weaker venting from the western rim of HtC3. HtC4 lies within and postdates HtC3, but HtC5–7 could have formed any time after HtC1 (and HtP1–3). HtC6 was possibly associated with the sector collapse between HtP2 and HtP3.

[16] The mesa-like edifice HtP3 is bounded by southeast dipping faults and, like HtP4 and HtP5 to the south, appears from backscatter imagery to be capped by lava flows. HtP4 has several vents controlled by ESE dipping faults and is separated from HtP5 by a northwest–southeast orientated graben-like structure containing northeast striking fissure ridges. Identifiable lava flows, scoria cones, and fissure ridges, plus the absence of pervasive faulting, suggests that HtP2–HtP5 result from constructional arc-front volcanism west of the calderas, and are not simply eroded remnants of the proto-Kermadec Ridge. The flat summits (Figure 2a, cross section c–d) could, in part, result from storm action, since they shoal to ~95–160 mbsl, well above the effective storm wave base [*Wright*, 2001]. Three small satellite cones to the northeast are faulted, with fissure ridges on the hanging walls; HtS1 and HtS2 are not strongly dissected or eroded, and are probably younger than HtS3, but all three probably predate the main eruptive phase.

[17] Dredging across the calderas (Figure 2a) yielded andesitic–dacitic scoriaceous blocks, bombs and lapilli, and minor rhyolitic pumice from the rim of HtC2 (dredge track 38); dacitic blocks (similar to those from HtC2) from the summit of HtR1 (dredge track 39); blocks of basaltic andesite (see Figure 3a) and some sulfide mineralisation from the summit and slopes of HtR2 (dredge tracks 40 and 41); and altered, blocky lava from the western wall of HtC3 (dredge track 42). Dredging was not attempted over the eastern highlands (HtP2–HtP5).

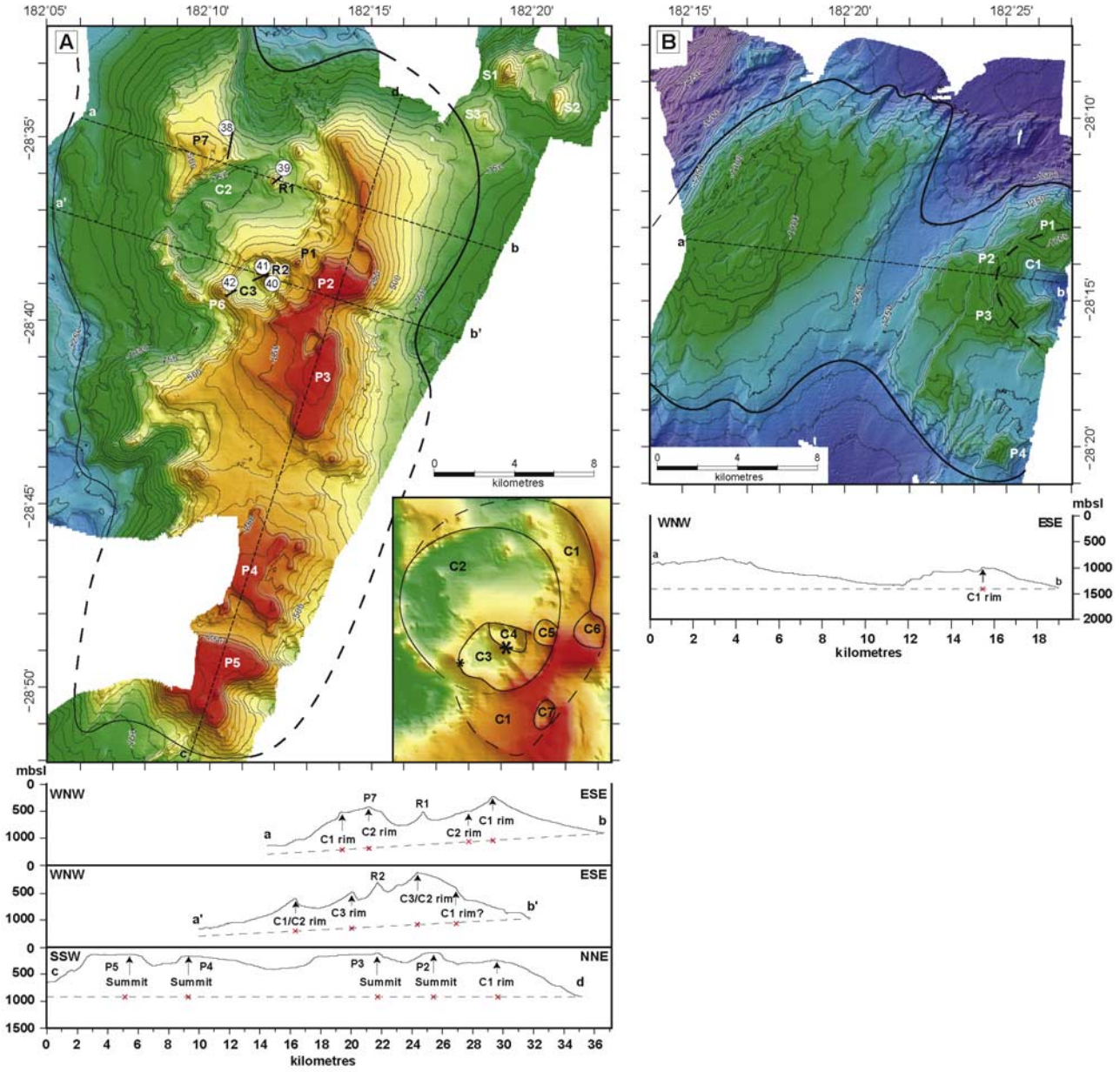

Figure 2. (a) Multibeam bathymetric map of Hinetapeka volcanic center. Nominal limits are shown by the thick connected line, and dredge tracks by the short black lines numbered 38–42. The inset shows the inferred caldera outlines, with asterisks denoting sites of active hydrothermal venting (the larger symbol indicating greater intensity) [*de Ronde et al.*, 2006]. The cross sections help define the outer limits of the center as well as the basal areas of edifices and their relief with respect to estimated baselines. The crosses on the baselines show the position of key peaks and troughs in the profiles above. (b) Multibeam bathymetric map of "OP."

[18] Recovered lavas are vesicular and glassy, with low phenocryst contents (Table 4). Whole-rock compositions (Appendix A) lie in the low-K tholeiite field of *Le Maitre* [1989], as do all other recovered NKST lavas (Figure 4a). The weighted mean composition of ~64 wt% is dominated by the large volume of HtC2 dacites relative to the minor, more primitive resurgent dome lavas (Appendix A). The compositional range of basaltic andesite to dacite (~56 to 68 wt% SiO_2; Table 5) is similar to that of the Raoul and Macauley volcanic centers to the south (Kermadec Islands; Figure 1a), which are likewise dominated by dacite.

4.2. "OP"

[19] "OP" is an incompletely mapped topographic high consisting of two edifices straddling the Kermadec Ridge crest (Figure 2b). The western edifice is ellisoidal and cut by numerous NNE striking, mainly ESE dipping faults and is a probable remnant of the proto-Kermadec Ridge. The eastern

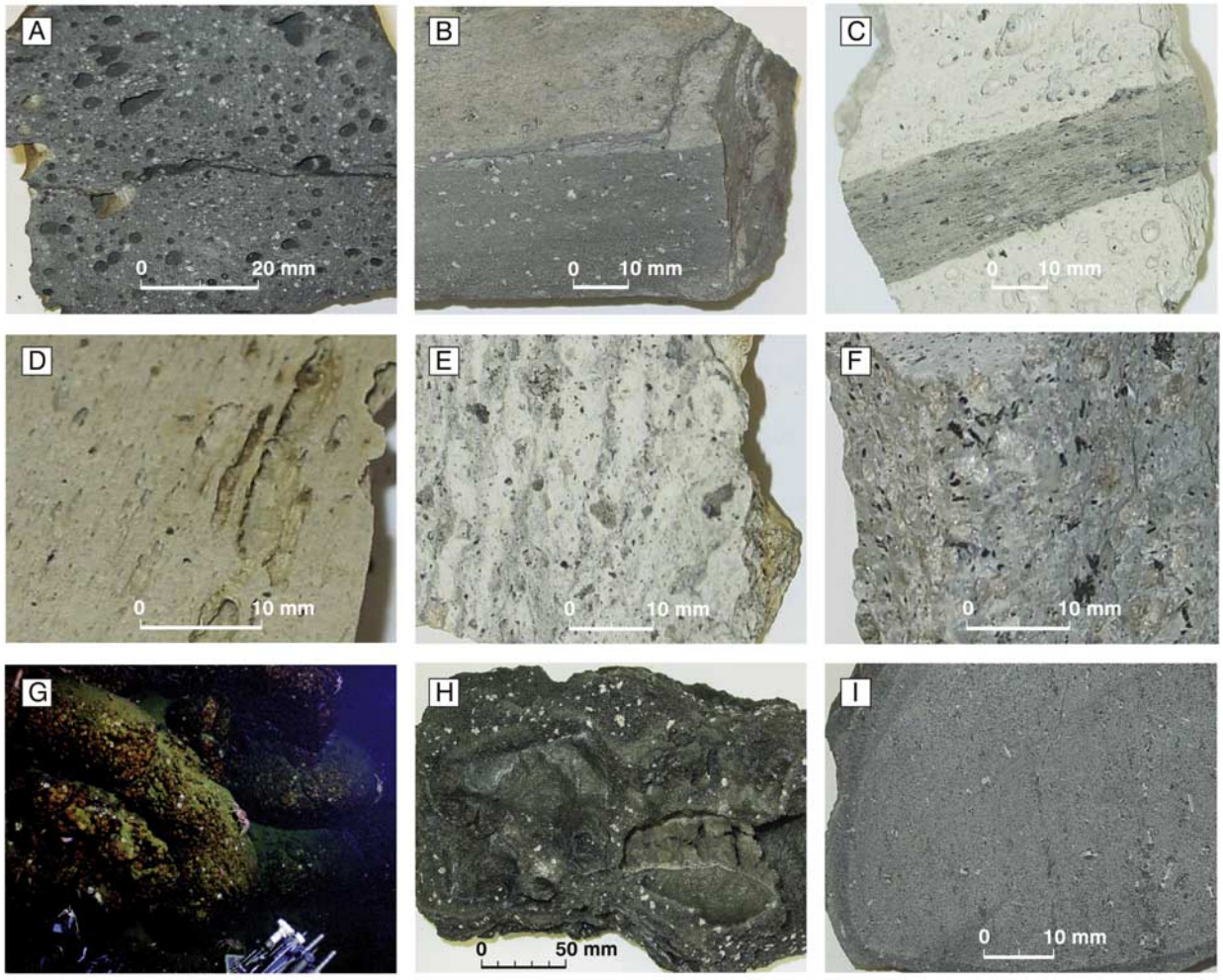

Figure 3. NKST lithologies: (a) Vesicular basaltic andesite from Hinetapeka (HtR2; sample P72512). (b) Laminated rhyolite from Gamble (GaV; P72456). (c) Pumiceous, glassy rhyolite from Gamble (GaV; P72450, similar to P72447–gray and white areas are chemically similar, but show different light reflectivity). (d) Woody textured, pumiceous glassy dacite from Rakahore (RkC2; P72429). (e) Pumiceous, mingled dacite with andesitic xenoliths from Hinepuia (HpV; P72360). (f) Holocrystalline rhyolite from Hinepuia (HpC2; P72403). (g) Pillowed lava at Monowai (western rim of MoC2). (h) Coarsely vesicular, glassy basalt from Monowai (MoV; P72271, similar to P72269). (i) Nonvesicular dacite from "U" (UC1; P72340).

edifice is less dissected, deeper, and has lower relief. Three cones (OPP1–3), cut by faults, line the rim of a caldera-like structure (OPC1) breached to the east. Another pyramidal shaped cone (OPP4) occurs to the south. The eastern edifice is cut by numerous NNE striking faults (WNW dipping in the west and ESE dipping in the south) and, although probably volcanic, showed no sign of hydrothermal activity [*de Ronde et al.*, 2006]. No dredging was attempted, and the status of "OP" as a volcanic center remains equivocal.

5. NKA Volcanic Centers

5.1. Putoto

[20] Putoto volcanic center (Figure 5a) comprises an ellipsoidal (northwest–southeast orientated), dome-like edifice with two slightly elongated summit calderas (PuC1, PuC2) and numerous parasitic cones, dikes, and fissure ridges (PuP2–PuP9). Sector collapse is widespread, with the most well-defined collapses occurring in the northwest, where headscarps are unmodified by later volcanic deposits. Faults are rare, occurring only to the east of PuP3, and dissecting the small satellite cone PuS1 to the west of the center. An elevated area to the southeast, dissected by numerous NNE striking, ESE dipping faults offsetting conjugate lineations, is interpreted to be a remnant of the proto-Kermadec Ridge.

[21] The two calderas have similar floor depths and relief (Table 3), and backscatter imagery shows significant sedimentation postcollapse. Like Hinetapeka, there is evidence of a general younging of volcanic features northwest to southeast across the center. In the northwest, both PuP1 and PuP10 are truncated on their southeastern sides, predating

Table 4. Petrography of Volcanic Center Lavas[a]

Volcanic Center	Vesicles[b] (%)	Phenocrysts[c] (%)	Glass[c] (%)	Olivine[c] (%)	Pyroxene[c] (%)	Plagioclase[c] (%)	Silica[c,d] (%)
Hinetapeka	19 (5–42)	10 (7–17)	43 (28–63)	0.2 (0–1)	15 (8–32)	25 (10–34)	5.2 (0–17)
Putoto	18 (1–62)	15 (0–39)	25 (1–64)	0.8 (0–3)	29 (6–53)	35 (16–60)	1.7 (0–7)
Gamble	38 (7–62)	4 (2–7)	68 (35–97)[e]	0.0	1 (1–2)	13 (1–38)	5.7 (0–23)
Rakahore	50 (43–63)	5 (4–7)	91 (88–95)	0.0	1 (1–2)	5 (3–6)	0.1 (0–0.3)
Hinepuia	36 (0–63)	27 (15–42)	53 (0–84)	0.3 (0–2)	10 (1–48)	21 (13–36)	2.0 (0–9)
Monowai	31 (12–57)	15 (1–34)	22 (0–65)	0.8 (0–2)	49 (19–74)	23 (12–39)	0.0
"U"	4 (0–13)	14 (7–21)	23 (0–56)	0.2 (0–1)	24 (2–48)	42 (34–55)	3.0 (0–8)
"V"	27 (19–34)	19 (3–38)	30 (2–56)	1.0 (0–2)	29 (20–51)	31 (19–45)	0.0

[a]From *Reyes* [2008].
[b]Calculated with respect to the total rock volume of lavas with <5% contamination.
[c]Calculated with respect to the total rock volume of lavas with <5% contamination, less vesicles.
[d]Tridymite or cristobalite (Hinetapeka, Putoto, Gamble, "U") or quartz (Rakahore, Hinepuia).
[e]Lithologies range from pumiceous (95–97% glass) to laminated (35–61% glass and up to 27% quench crystallites).

PuC1. Three postcollapse cones within PuC1, aligned subparallel to the calderas, have in-filled craters. The western, shared rim of PuC2 postdates PuC1 formation. Within PuC2, the larger cone of a coalescing pair has an active crater and, together with several smaller cones, forms a north-trending lineament that includes PuP5 on the southern rim of PuC2 and several small cones on the northern rim of PuC2. Strong hydrothermal venting from the southern wall of PuC2 (Figure 5a inset), and the presence of lava flows extending from PuP5 into PuC2, indicates this lineament is the locus of recent volcanism. Weak hydrothermal venting from near PuR1 suggests that the collapse of PuC1 and formation of resurgent domes occurred immediately precollapse of PuC2.

[22] Recovered lithologies include andesitic–dacitic lapilli and scoria from the northeastern rim of PuC1 (Figure 5a; dredge track 35); blocky basaltic lava from the northern wall of PuC1 and the southern slope of PuP1 (dredge track 36); andesitic cobbles and scoria from the summit and slopes of PuR1 (dredge track 37); and blocky basaltic lava and scoria from the summit and slopes of PuP5 (dredge tracks 33 and 34). Compared with Hinetapeka, Putoto lavas are less glassy and vesicular, more phenocryst-rich (Table 4), and cover a wider compositional range extending to lower silica contents (~50–65 wt% SiO_2; Table 5). The lower weighted mean composition of ~54 wt% SiO_2 reflects dominance of late-stage basaltic lavas from PuP5.

5.2. "Q"

[23] Between Putoto and Gamble volcanic centers lies an eroded edifice, "Q" (Figure 5b), which has a subdued morphology and is probably a remnant of the proto-Kermadec Ridge. "Q" shows no strong evidence for recent volcanism except, possibly, for a small cone that rises to ~1000 mbsl near its center. The southern and eastern flanks are pervasively cut by north to NNE striking, east dipping faults. Backscatter imagery indicates exposed basement on the steeper western and eastern flanks.

5.3. Gamble

[24] Gamble volcanic center (Figure 6a) is broadly ellipsoidal (northwest–southeast orientated) and covers an area significantly larger than Putoto but with a smaller volume (Table 1). The center comprises a large, active cone complex (GaV) of similar summit height and relief to Putoto, two nested caldera-like structures (GaC1 and GaC2), and a number of parasitic cones (GaP1–9). In the northwest is a vent field with several small parasitic cones, one of which (GaP9) is a site of recent volcanism. Northwest of GaP9, smaller cones and fissure ridges lie along northeast striking, southeast dipping faults. To the east is a strongly dissected edifice cut by numerous north to northeast striking faults (southeast dipping in the west and northwest dipping in the east), interpreted to be part of the proto-Kermadec Ridge (Figure 1b).

[25] GaV has several craters, each showing sector collapse. Plume surveying [*de Ronde et al.*, 2006] indicated intense hydrothermal venting from the summit. The large breach west of the summit has displaced a substantial part of the original edifice downslope to the southeast. The parasitic cones GaP1 and GaP2 on the northern flank occupy a narrower area of sector collapse bounded to the east by northeast striking, southeast dipping faults. The older of the two calderas (GaC1) is strongly ellipsoidal, orientated east–west. The southern rim, breached by sector collapse, is partly defined by a string of small cones striking ESE, whereas the postcollapse cone GaP8 defines the northern rim and GaV the eastern rim, respectively. GaC2 is nested within GaC1 and is orientated northwest–southeast.

[26] Dredging across the summit and northern slope of GaV (Figure 6a; dredge tracks 30–32) yielded large amounts of blocky lava and some sulfide-rich minerals from near the site of hydrothermal venting. Attempts to dredge the eastern rim (dredge tracks 31a and 32a) and the southwestern rim (dredge track 32b) of GaC2 were unsuccessful. Sampled lithologies, in subequal proportions, included gray laminated rhyolite (Figure 3b) and white and gray pumiceous rhyolite (Figure 3c). No mafic compositions were recovered, except for occasional andesitic xenoliths. The lavas are highly vesicular and glassy, with modest phenocryst contents (Table 4). Whole-rock compositions range narrowly (72.4–74.4 wt% SiO_2; Appendix A), and there is no compositional distinction between the two main lithologies.

5.4. Rakahore

[27] Rakahore volcanic center (Figure 6b) consists of an ellipsoidal (northwest–southeast orientated), dome-like edifice with nested summit calderas breached to the southwest. Extensive vent fields and fissure ridges striking generally northeastward form the lower flanks and outer margins.

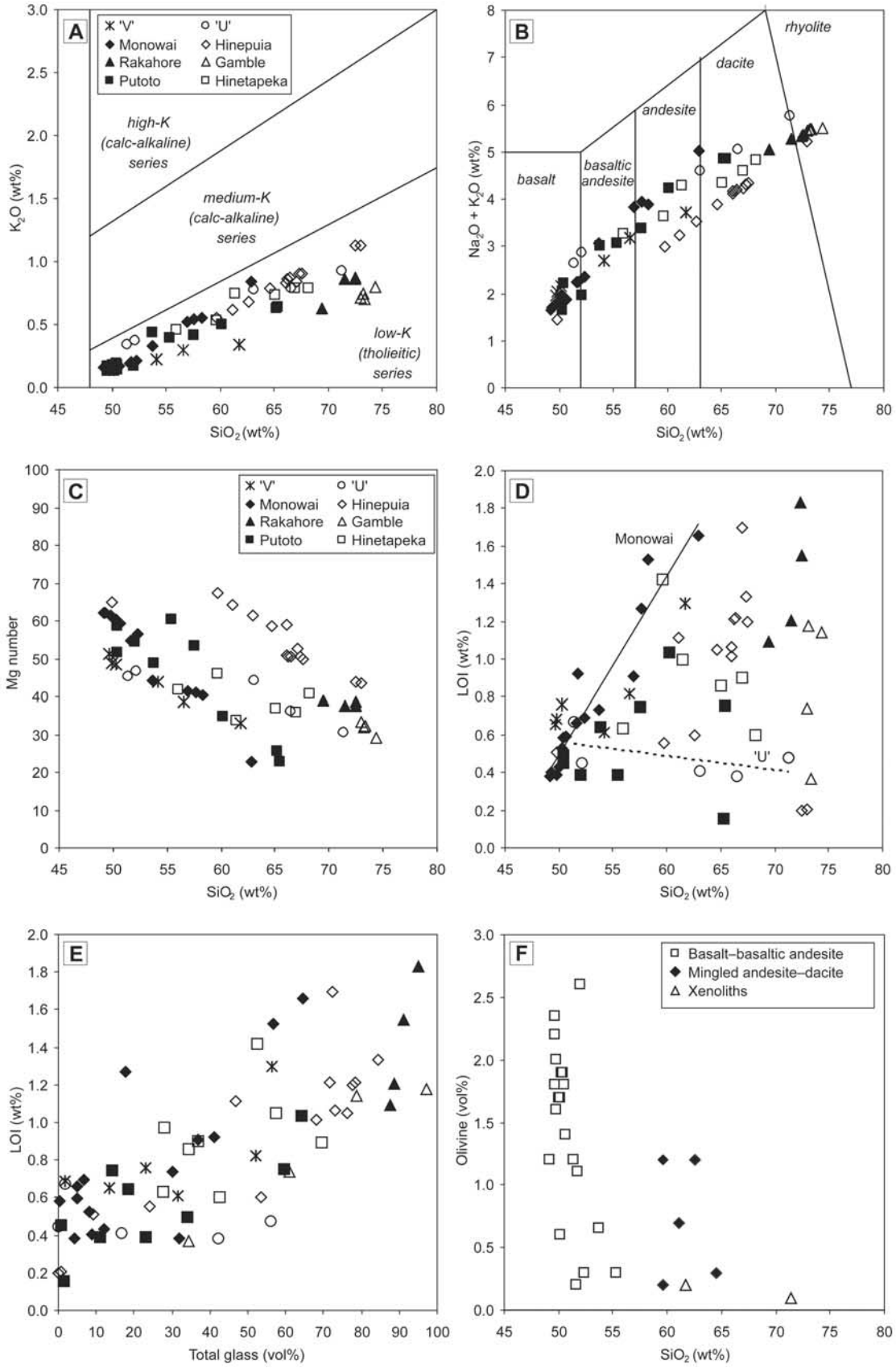

Figure 4. Whole-rock variation diagrams: (a) K_2O versus SiO_2–fields after *Le Maitre* [1989]. (b) Na_2O + K_2O versus SiO_2–fields after *Le Maitre* [1989]. (d) Mg-number (100 Mg/(Mg + Fe)) versus SiO_2. (d) LOI versus SiO_2. (e) LOI versus total glass. (f) Olivine versus SiO_2.

Table 5. NKST Lithologies

	Depth[a] (mbsl)	Basalt	Basaltic Andesite	Andesite	Dacite	Rhyolite	Bulk-Rock Silica (wt%) Range[b]	Mean[b,c]
Hinetapeka	617	0	1	2	3	0	56.0–68.2	64.1
Putoto	443	2	3	2	2	0	50.4–65.4	54.3
Gamble	442	0	0	0	0	4	72.4–74.4	73.2
Rakahore	766	0	0	0	2	2	69.4–72.5	71.5
Hinepuia	379	1	0	3	8	2	49.8–72.9	64.0
Monowai	718	10	3	3	0	0	49.2–62.9	52.7
"U"	351	1	1	0	2	1	51.4–71.3	59.8
"V"	731	3	2	1	0	0	49.6–61.8	55.5
Volume-weighted		13%	16%	21%	33%	17%		61.9

[a]Volume-weighted mean depth of sampling sites (meters below sea level).
[b]Samples with <5% contamination (xenoliths plus alteration minerals).
[c]Volume-weighted.

Those to the west have prominent linear segments up to 2.5 km long which, from backscatter imagery, are recent lava flows emanating from fault footwalls. Faults strike north to northeast and dip to the east. One ~15 km-long trace strikes 060° through RkC2 and appears to postdate caldera collapse. To the northeast, a probable remnant of the proto-Kermadec Ridge (Figure 1b) is extensively cut by NNE striking, WNW dipping faults.

[28] The calderas (RkC1 and RkC2) are both subcircular and contain resurgent domes and postcollapse parasitic cones (RkP1–RkP4) on their southern and western rims. A narrow breach of the southeastern caldera wall coincides with a vent field containing cones and fissure ridges.

[29] Dredging across caldera walls and rims (Figure 6b; dredge tracks 26–29) yielded subequal amounts of blocky, pumiceous, often woody-textured dacite (Figure 3d), and blocky, pumiceous rhyolite. No rocks of more mafic composition were recovered. Some altered and Fe-stained lavas from near the source of weak hydrothermal venting (Figure 6b inset) were sampled.

[30] All recovered lavas are highly vesicular and glassy, with very low phenocryst contents (Table 4). Andesitic xenoliths are common (≤15%; Appendix A). Whole-rock compositions range narrowly, with lower SiO_2, Mg number and LOI than Gamble lavas, but similar K_2O and total alkalis (Figures 4a and 4b).

5.5. Hinepuia

[31] Hinepuia volcanic center (Figure 6c) is an irregularly shaped, complex system consisting of two northwest–southeast aligned edifices separated by nested calderas (HpC1 and HpC2). The southeastern edifice (HpV) is an active cone complex with multiple craters. The northwestern edifice (HpP6–HpP8) is older, with a more subdued topography dissected by faults. In the southeast, a faulted parasitic cone (HpP4) forms a lineament with HpP3, on the southern rim of HpC1, and the two main vents of HpV. In the north an extensive vent field is aligned northeast–southwest along the hanging walls of southeast dipping faults. HpV is associated with recent volcanic activity, and strong hydrothermal plumes vent from the summit region [*de Ronde et al.*, 2006].

[32] Remnant caldera rims east of HpP7 suggest that caldera activity has migrated southeastward across the center. The oldest clearly defined caldera, HpC1, is ellipsoidal (east–west orientated) and has sustained significant sector collapse along its western rim, possibly during formation of HpC2. Low backscatter reflectivity indicates that the caldera floor is sedimented. HpC2 is subcircular and has a number of postcollapse cones along its rim including HpV. Several cones within HpC2 are aligned east–west and two, including HpR1, have summit craters. Faults are pervasive in the northwest, where they strike northeast, dipping to the southeast, or strike NNE dipping to the WNW, but are rare in the younger, eastern parts around HpC2 and HpV. To the south, occasional faults strike northeast and mainly dip to the southeast.

[33] Only the younger, eastern parts of Hinepuia were dredged (Figure 6c; dredge tracks 20–25), yielding pumiceous, blocky, mingled andesite–dacite (Figure 3e), minor blocky, holocrystalline rhyolite (Figure 3f), and rare basalt. The andesites–dacites have similar degrees of vesicularity to Gamble and Rakahore lavas, but less glass and more phenocrysts (Table 4). Disequilibrium mineral assemblages and textures are common, including xenoliths (≤9%; Appendix A). Xenoliths are mainly basalt–andesite, but include microdiorite and, rarely, rhyolite.

[34] The andesite–dacite compositions range narrowly (~60–67.5 wt% SiO_2; Appendix A), with a weighted mean of ~64 wt% SiO_2. The weighted mean compositions of HpC2 and HpV are broadly similar (~67 and 64 wt% SiO_2, respectively), suggesting that the caldera and dome complex may be coeval, with HpV representing postcollapse resurgence from a common reservoir. Correlations of major elements (Figures 4a and 4b) and Mg number (Figure 4c) are tight and linear, the latter plotting above the other NKST trends.

6. STA Volcanic Centers

6.1. Monowai

[35] Monowai volcanic center (Figure 7a) comprises two calderas (MoC1 and MoC2), a large stratovolcano (Monowai volcano, MoV), and a number of parasitic cones. Although its full extent to the west and east is unknown, the center as mapped is slightly elongated (northwest–southeast orientated) and covers an area similar to Hinetapeka, with a volume similar to that of Gamble (Table 1).

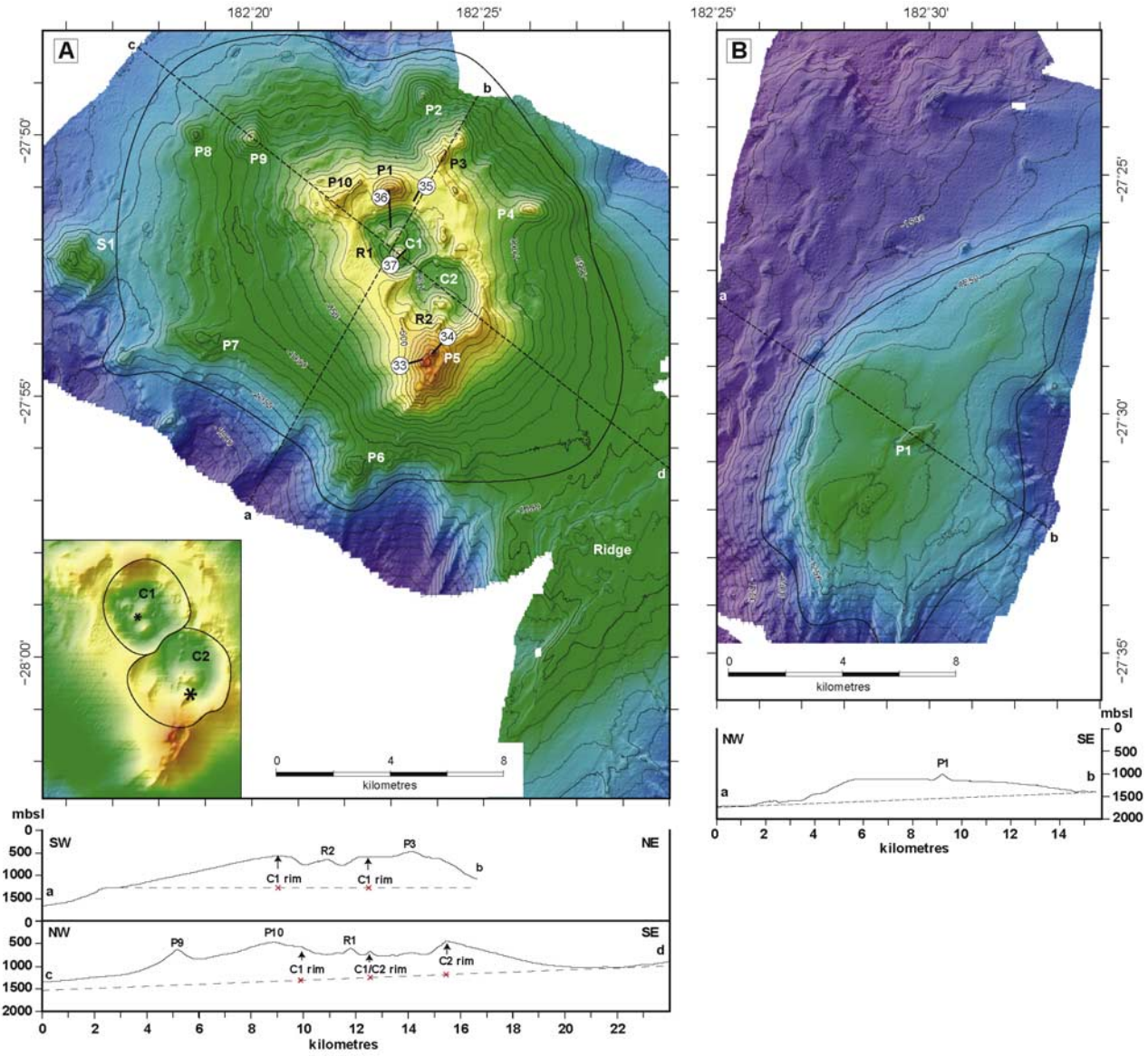

Figure 5. Multibeam bathymetric maps and cross-sections of (a) Putoto volcanic center and (b) "Q."

[36] Parasitic cones in the west (MoP6–8) are variably dissected by faults and predate MoV and caldera formation. MoP7 is a possible resurgent dome within a remnant caldera structure whose bathymetry has been severely modified by sector collapse and faulting and whose floor is largely infilled by sediment. The oldest clearly defined caldera, MoC1 has by far the largest volume of any NKST caldera (Table 3). Its rims contain a number of precollapse cones dissected by caldera ring faults and/or subsequent caldera wall collapse. An intact cone on the southwestern rim (MoP5) formed postcollapse. The remnant floor of MoC1 shows low backscatter reflectivity, indicating sediment infilling. MoC2 is entirely nested within MoC1, elongated slightly more toward the south. It has an almost flat floor, near the center of which is a resurgent dome (MoR1). Rotational block slides within the caldera wall, along ring faults, have provided pathways for postcollapse magma extrusion. Numerous small cones have erupted on both the hanging wall and footwall of these faults.

[37] MoV is a cone-shaped stratovolcano with a constructional volume of ~11 km^3. Slope morphology indicates widespread localized sector collapse; recent collapse of the upper southern slope between 1998 and 2004 was followed by regrowth of a 155 m cone, the site of ongoing volcanic activity [*Wright et al.*, 2008]. MoV does not have an obvious summit crater, but intense hydrothermal venting and eruptions from the summit have been recorded since 2002 [e.g., *de Ronde et al.*, 2006].

[38] Faults are pervasive in the north and west, where they strike NNE and dip to the ESE forming rotated fault blocks back-tilted to the northwest. Near the western rim of MoC1, southeast striking faults may, in part, have caused collapse of the caldera wall. Most regionally aligned faults terminate at the caldera rims, which are controlled by ring faults.

[39] Monowai has been well sampled since its discovery in 1978 [*Davey*, 1980], with the 1998 *Sonne* expedition extensively dredging the summit and western slopes of

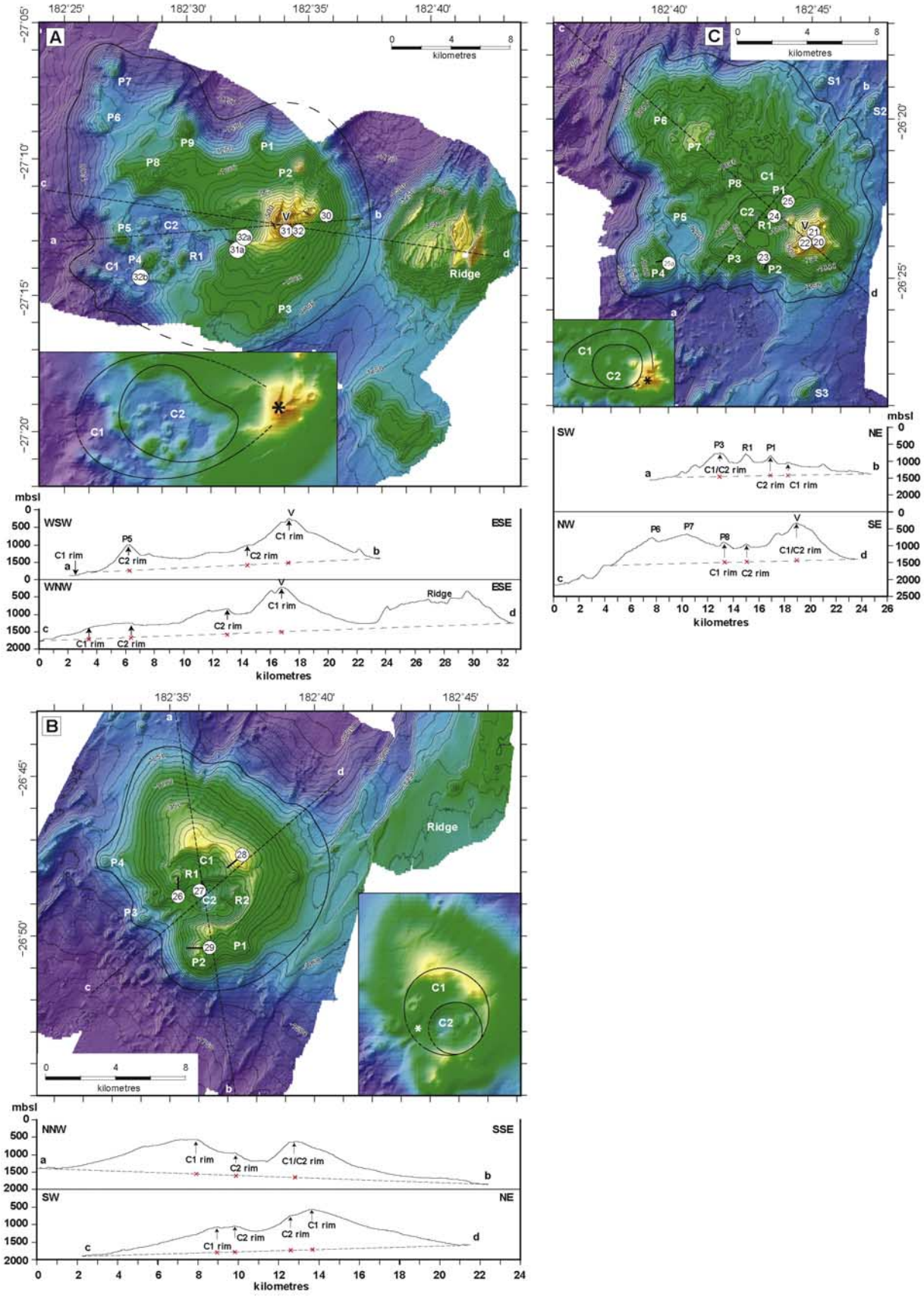

Figure 6. Multibeam bathymetric maps and cross sections of (a) Gamble volcanic center, (b) Rakahore volcanic center, and (c) Hinepuia volcanic center.

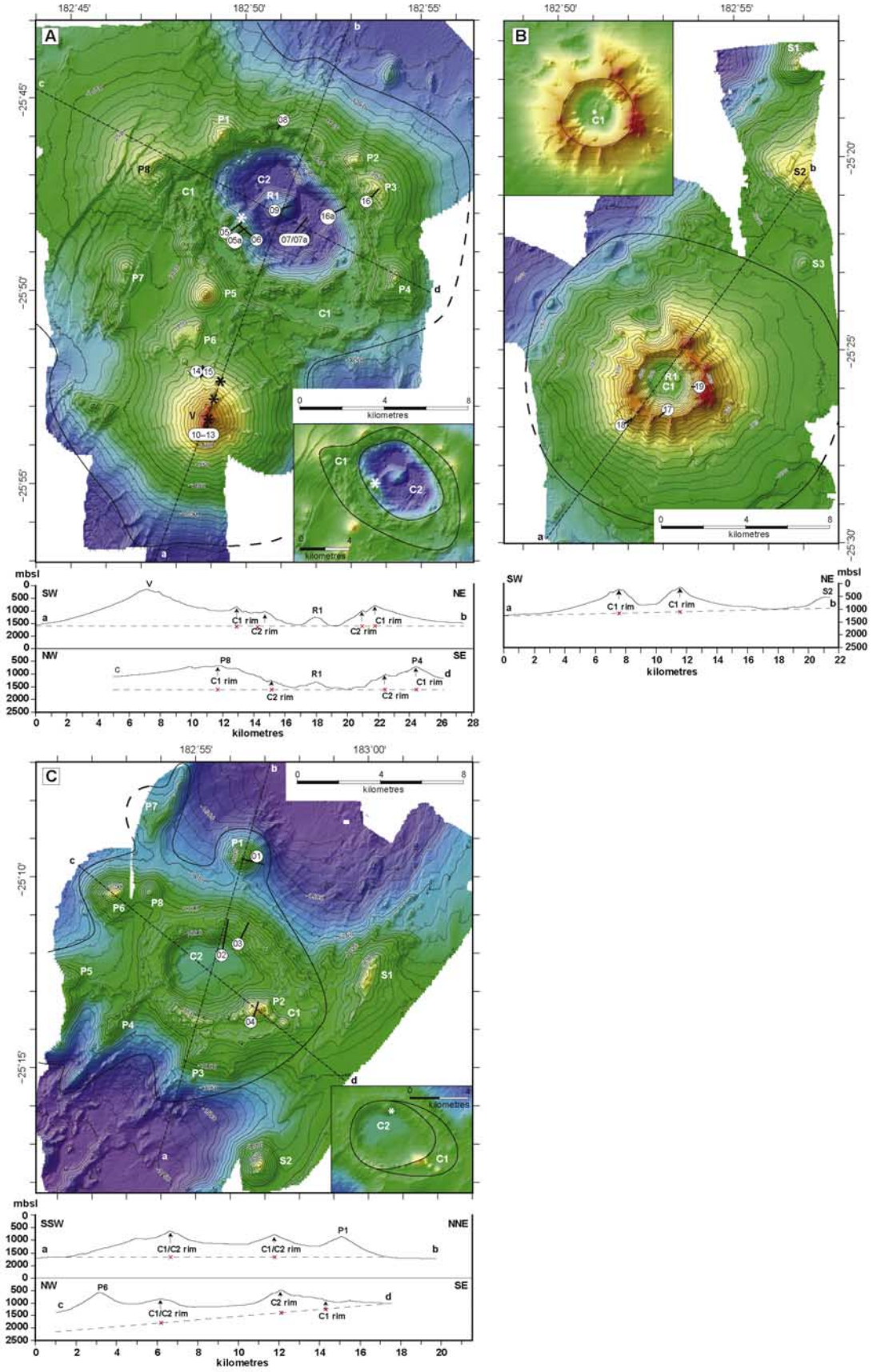

Figure 7. Multibeam bathymetric maps and cross sections of (a) Monowai volcanic center, (b) "U" volcanic center, and (c) "V" volcanic center.

MoV [*Haase et al.*, 2002], and the 2004 NZAPLUME III expedition undertaking 14 dredge tows across various parts of the center, including the newly discovered calderas (Figure 7a). Recovered lavas range from blocky, sometimes pillowed lava to cobbles and scoriaceous cinders. Apart from native sulfur from the summit of MoV, the product of very recent eruptive activity, and some weakly altered lava from the northern wall of MoC1, recovered samples were pristine, with many exhibiting fresh, glassy rims. Attempts to dredge the floor of MoC2 (dredge tracks 07 and 07a) and the eastern wall of MoC1 (dredge track 16a) were unsuccessful. A 2005 Pisces V dive expedition [*Embley et al.*, 2006] revisited the western rim of MoC2 recovering samples of blocky and pillowed lava (Figure 3g).

[40] Lithologies include basaltic andesite from the eastern rim of MoC1 (dredge track 16); sparsely porphyritic basalt from the northern slope of MoV (dredge tracks 14 and 15); coarsely porphyritic basalt from the summit of MoV (dredge tracks 10–13; Figure 3h); sparsely porphyritic basalt to basaltic andesite from the northern wall of MoC1 (dredge track 08) and MoR1 (dredge track 09); and andesite from the western rim of MoC2 (dredge tracks 05 and 06).

[41] The lavas are vesicular and glassy (Table 4), particularly the most recent eruptives from MoV. Whole-rock compositions range from ~49 to 63 wt% SiO_2, with a weighted mean of ~53 wt% SiO_2. Although Monowai is well sampled, lavas with higher silica contents (i.e., >63 wt% SiO_2) were not recovered. The stratovolcano and the calderas have mutually exclusive compositional ranges (Appendix A), with MoV being entirely basaltic (weighted mean ~50 wt% SiO_2) and MoC1/MoC2 being basaltic–andesitic (weighted mean ~55 wt% SiO_2). Overall, compositions trend with increasing SiO_2 toward higher K_2O, total alkalis and LOI, and lower Mg number than other NKST lavas (Figure 4). The high volatile (Figure 4d) and glass (Figure 4e) contents of Monowai andesites, explosively erupted, might explain the formation of calderas in the absence of more evolved compositions.

6.2. "U"

[42] "U" volcanic center (Figure 7b) is a noncomplex, unfaulted, conical edifice with a central caldera (UC1). Three small satellite cones occur to the north, the largest of which (US2) is dissected on its northwestern flanks by northeast striking northwest dipping faults and may be a remnant of the proto-Kermadec Ridge.

[43] UC1 shoals to ~142 mbsl, similar to the summit of MoV, and is the deepest caldera in the NKST sector, with relief of 665 m (Table 3). The outer flanks are dissected by large sector collapses spaced at regular intervals and bounded by radial dikes that form structural ribs. The most prominent sector collapse, in the northwest, includes density flow bed forms.

[44] The caldera walls and rim comprise angular blocks of basaltic to rhyolitic lava, with minor pumice. In contrast to other NKST lavas, "U" lavas are typically nonvesicular (Table 4; Figure 3i) and contain few quench textures, indicating effusive eruption. This is consistent with the high, steep walls of the caldera, and the blocky, generally glass-poor nature of the lavas. Whole-rock compositions range widely (~51–71 wt% SiO_2; Appendix A), with the weighted mean of ~60 wt% SiO_2 indicating an even compositional spread across the center.

6.3. "V"

[45] The smallest of the NKST volcanic centers, "V" has an irregular, broadly ellipsoidal (northwest–southeast orientated) shape and a subdued edifice topography (Figure 7c). It comprises two nested calderas (VC1 and VC2), a number of parasitic cones and fissure ridges (VP1–VP8), and multiple lava flows and dikes. There is no evidence for faulting, except along the western margin of the fissure ridge VP7. The caldera rims have uneven topography, with the southeastern and southern rims marked by parasitic cones. There is no evidence of sector collapse, suggesting that volcanic activity persisted postcaldera formation.

[46] To the east, two satellite edifices align subparallel to the regional tectonic fabric. VS1 is a fissure ridge that extends northeastward into a vent/fissure ridge field associated with northwest dipping faults. VS2 is a scoria cone showing sector collapse on its western flank. To the southwest of VC2, fissure ridges bound a zone of extensive flank collapse leading to a vent field. In the north are two east–west aligned parasitic cones (VP6 and VP8), a northeast striking fissure ridge (VP7), and another parasitic cone (VP1) with lava flows and radial dikes extending from its flanks. All have summit craters. Evidence from backscatter imagery of lava flows covering much of the outer flanks, the generally pristine morphology, and the lack of pervasive faulting indicates extensive recent volcanism across much of the center.

[47] Recovered lithologies include andesitic lapilli and scoriaceous cobbles from the northeastern wall and rim of VC2 (Figure 7c; dredge tracks 02 and 03); basaltic andesite and altered dacitic? blocks and scoria with native sulfur and pyrite from the southeastern rim of VC2 (dredge track 04); and basaltic blocks and scoria, and minor rhyolitic pumice from the summit and eastern slope of VP1 (dredge track 01). Although the compositional range is similar to that of Putoto and Monowai, K_2O concentrations at equivalent SiO_2 content are lower (Figure 4a). The northern floor of the caldera comprises ferromanganese-rich crusts, indicating extensive hydrothermal venting (Figure 7c inset), consistent with poor preservation of recovered samples.

7. Discussion

[48] NKST volcanic centers have formed on, or immediately to the west of, the Kermadec–Tonga Ridge crest. Trench rollback over the past ~5 Ma [*Wright et al.*, 1996] has caused the proto-Kermadec–Tofua Arc to rift, with concomitant back-arc extension in the Havre Trough. As the arc has evolved, the NKST subarc crust has become a collage of hydrothermally altered protoarc crust (volcanic and plutonic equivalents of subduction-related lava), augmented by underplating and eruptive products, and attenuated by back-arc extension [e.g., *Ewart et al.*, 1994], to a thickness of 16–19 km [*Shor et al.*, 1971].

[49] Faulting is pervasive both along the Kermadec Ridge, and within older parts of the NKST centers. Fault strikes typically lie between 020° and 060° with a unimodal distribution around 045° oblique to the regional basin trend of the northern Havre Trough by ~025°. A change in fault

strike along the arc is consistent with oblique rifting along the southern and middle sectors of the arc [*Campbell et al.*, 2007] and the regional anticlockwise rotation of T axes [e.g., *Pelletier and Louat*, 1989]. Such faulting controls the structural construction of arc edifices and regional tectonic permeability along the arc front.

[50] Within this context, we now discuss specific aspects of NKST magma ascent and emplacement, eruptive style, and magma degassing.

7.1. Arc Magmatism

[51] New multibeam mapping and sampling of the NKST arc segment provides further evidence of voluminous and widespread silicic caldera volcanism as a major component of intraoceanic arc magmatism. For the Kermadec and southern Tofua arcs (*Wright and Gamble* [1999], *Wright et al.* [2006], *Stoffers et al.* [2006], and this study), it is apparent that silicic caldera volcanism, at least for the past 500 ka, is the dominant eruptive style at the arc front for more than 1000 km north of ~32°S. To the south, basaltic–andesitic volcanism is dominant, even in the SKA sector south of 34°S, which includes three silicic calderas.

[52] For the Kermadec arc as a whole the relative volumes of effusive basaltic and pyroclastic silicic is bimodal [*Wright et al.*, 2006], with 30–50% of arc construction being dacitic–rhyolitic (>63% wt% SiO_2). Such bimodality, and the presence of voluminous, silicic, caldera-sourced eruptives, is recognized from other intraoceanic arcs including Izu-Bonin [*Yuasa et al.*, 1991; *Tamura and Tatsumi*, 2002], south Sandwich [*Leat et al.*, 2007], and central Vanuatu [*Robin et al.*, 1993], and where imaged by wide-angle seismic experiments, coincide with midcrustal layers with *P* wave velocities of 6–6.5 km s^{-1} [*Crawford et al.*, 2003; *Leat et al.*, 2003; *Kodaira et al.*, 2007] that are interpreted as felsic intrusives. Two end-member models of either fractional crystallization of basaltic magma [e.g., *Pearce et al.*, 1995] or crustal anatexis [*Tamura and Tatsumi*, 2002; *Smith et al.*, 2003b] have been proposed for the generation of these silicic magmas. For intraoceanic arcs in general, and the Kermadec–Tofua arc in particular, the sheer volumetric scale of silicic eruptives and the heterogeneity of silicic magmas at given SiO_2 abundances, even from the same center (e.g., Raoul volcanic center), has suggested that partial melting of subarc crust is the dominant process operating [*Smith et al.*, 2003a, 2003b, 2006].

[53] The NKST volcanic centers exhibit a broad range of lava compositions, with volume-weighting (Table 5) indicating a skew toward dacite. Although there is no systematic variation with either water depth or latitude, there is a tendency toward more silicic lavas in the middle, deeper NKA sector (at least with respect to the most recent volcanism). Apart from the reconnaissance work of *Shor et al.* [1971], there is a dearth of modern shipborne gravity anomaly and seismic refraction data along this part of the arc with which to document lateral variations in crustal structure. Accordingly, the geophysical and crustal structure of the northern Kermadec arc remains an open question. The Louisville Ridge intersects with the Tofua Arc immediately north of the NKST sector and is interpreted as having no significant effect on magma composition or eruptive style.

[54] All lava compositions lie within the low-K tholeiitic field of *Le Maitre* [1989] (Figure 4a), with most basalts being high-alumina types containing olivine + plagioclase + clinopyroxene±orthopyroxene and ≥16.5 wt% Al_2O_3 [*Crawford et al.*, 1987]. Individual centers typically show single, well-defined major element trends (Figures 4a–4c) indicating monogenetic magmatic histories. Major element chemistry, mineralogy and disequilibrium textures provide pointers to the dominant processes operating, such as magma mixing at Hinepuia and crystal fractionation at Monowai. However, an in-depth analysis using trace element and isotopic data, and analysis of melt inclusions, is beyond the scope of this paper and will be reported separately.

7.2. Magma Emplacement

[55] The main NKST volcanic edifices lie between major fault sets, which typically change strike direction (e.g., Rakahore, Hinepuia, "V") and/or dip direction (e.g., Hinetapeka, Gamble, Rakahore, "U") across each center. Dike orientation, as manifested by fissure ridge, vent cone, and fault alignments is predominantly northeast, orthogonal to the ~120–140° extension trend [e.g., *Pelletier and Louat*, 1989; *Parson and Wright*, 1996] and consistent with volcanic edifice emplacement controlled by local tectonic stress regimes [*Watanabe et al.*, 1999]. Caldera elongation and orientation often reflects magma chamber geometry [*Acocella et al.*, 2002], which in itself can be a function of the regional stress field [e.g., *Holohan et al.* 2004, 2008].

[56] Over half the NKST calderas are elongate with long-axis trends lying between 090 and 150° (mean 117°), nearly orthogonal to the Havre Trough rift extension direction and intrarift basement fabric. Such caldera elongation is common along the Kermadec [*Wright et al.*, 2006] and Tofua arcs [e.g., *Stoffers et al.*, 2006] and reflects the underlying control of back-arc extension on the wider arc front. For individual centers though, most strain is taken up by magmatic accommodation [*Parsons et al.*, 1998]. Within such strain accommodation zones, deformation increases permeability and fluid flow [*Rowland and Sibson*, 2001], aiding magma ascent and hydrothermal fluid flow. Extensional magmatic accommodation is not dominantly fault-controlled but involves significant dike intrusion via the development of rift grabens [*Parsons et al.*, 1998]. In the SKA sector (Figure 1a), *Wright et al.* [1996] suggest that arc volcanism limits rift development, acting as a barrier to longitudinal arc-parallel fault propagation, as the arc front migrates west to east, and with arc-front volcanoes between rift-segments. Analogous arc edifice and intervolcano rift development has been identified from many active arc–rift systems including the continental Taupo Volcanic Zone [*Rowland and Sibson*, 2001] and the Izu–Bonin arc [*Taylor et al.*, 1991]. For the NKST arc segment, we similarly interpret the pattern of faulting as evidence that the major volcanic centers are "soft linkage" zones between incipient rift faulting.

7.3. Magmatic Evolution and Eruptive Style

7.3.1. Mineralogy

[57] Nearly all recovered NKST lavas are porphyritic, most are glomerocrystic and a few are vitrophyric. "Dry" phenocryst assemblages (Table 6; Figures 8a and 8e) are

Table 6. Summary of NKST Petrography[a]

	Basalt–Basaltic Andesite–Andesite (<60 wt% SiO_2)				Andesite–Dacite–Rhyolite (≥60 wt% SiO_2)			
	Count[b]	Minimum (vol%)[c]	Maximum (vol%)[c]	Mean[d] (vol%)[c]	Count[b]	Minimum (vol%)[c]	Maximum (vol%)[c]	Mean[d] (vol%)[c]
Vesicles[e]	32	0.1	57.1	23.7	30	0.0	63.2	33.1
Xenoliths[e,f]	2	0.0	2.0	0.1	12	0.0	4.0	0.6
Phenocrysts[g,h]	32	2.6	38.7	17.4	32	0.4	41.7	14.0
Groundmass[g,i]	32	7.8	89.3	61.1	32	0.5	93.4	21.5
Glass[g]	31	0.0	56.9	19.6	32	0.1	97.3	58.6
Crystallites[g,j]	2	0.0	41.9	1.9	17	0.0	57.1	6.0
Olivine[g]	21	0.0	2.6	0.9	5	0.0	1.2	0.08
Pyroxene[g]	32	8.9	74.3	41.7	32	0.8	24.5	7.5
Plagioclase[g]	32	9.9	49.2	29.0	32	1.2	59.5	21.1
Fe-Ti oxide[g]	32	0.1	17.3	6.1	32	0.2	7.4	2.5
Apatite[g]	3	0.0	0.4	0.03	15	0.0	1.7	0.14
Quartz[g]	0	0.0	0.4	0.01	12	0.0	9.2	0.8
Tridymite[g] or Cristobalite[g]	5	0.0	4.8	0.24	9	0.0	22.6	2.4
Hornblende[g]	0	0.0	0.0	0.0	2	0.0	2.9	0.17
K-feldspar[f]	0	0.0	0.0	0.0	1	0.0	0.2	0.01
Secondary minerals[f]	23	0.0	4.2	0.6	24	0.0	3.7	0.7

[a]From *Reyes* [2008].
[b]The number of samples in which the phase or feature was detected.
[c]Modal analysis.
[d]Calculated with respect to the full sample set ($\Sigma = 32$).
[e]Calculated with respect to the total rock volume of lavas with <5% contamination.
[f]All components included in general percentages.
[g]Calculated with respect to the total rock volume of lavas with <5% contamination, less vesicles.
[h]Includes glomerocrysts, crystal aggregates, and microphenocrysts.
[i]Here,100 − phenocrysts − crystallites.
[j]Unidentified microphenocrysts (includes the quartzo-feldspathic matrix of Hinepuia rhyolite).

typical of volcanic arcs globally, and similar to those of other Kermadec arc sectors [*Gamble et al.*, 1993, 1995, 1997; *Worthington et al.*, 1999; *Smith et al.*, 2003a, 2003b, 2006]. Basaltic to andesitic lavas (<60% SiO_2) are dominated by plagioclase and pyroxene (clinopyroxene plus subordinate orthopyroxene), which collectively account for more than 70% of most lava compositions. Glass (mean 20%), Fe-Ti oxides (mean 6%, mainly titanomagnetite and ilmenite), olivine (mean 1%), and occasional apatite comprise the remainder. Andesitic to rhyolitic lavas (≥60% SiO_2) are dominated by glass (mean 59%), with plagioclase (mean 21%), pyroxene (mean 7.5%, orthopyroxene dominating over clinopyroxene with increasing silica content), Fe-Ti oxides (mean 2.5%, mainly titanomagnetite and ilmenite), tridymite/cristobalite (mean 2.4%), quartz (mean 1%), apatite (mean 0.1%), and indeterminate crystallites (mean 6%) comprising the remainder. Hornblende and alkali feldspar occur only in the Hinepuia rhyolite.

[58] Olivine occurs in 41% of samples (20 of 32 basalts–andesites and 7 of 32 andesites–dacites–rhyolites) and ranges to 2.6% (Figure 4f). In andesites–dacites–rhyolites, two occurrences are xenocrystic showing resorption and/or Fe-Ti oxide ± pyroxene reaction rims (Figure 8b), and the remainder are forsteritic phenocrysts (Fo_{79-82}) in mingled andesites–dacites. Many, though not all, have thin reaction rims and are accompanied by quartz phenocrysts. Electron probe (EPMA) data [*Peckett*, 2006] show olivine phenocrysts in basalts and basaltic andesites to be moderately forsteritic (Fo_{60-81} in two samples from "U" and "V"). Crystals are often skeletal (46%) or have resorbed margins (29%) or reaction rims (53%). Only two whole-rock compositions (both from Monowai) are olivine-normative, so resorption and reaction with the melt is not unexpected [*Peck et al.*, 1966]. However, most olivine phenocrysts in Monowai lavas are euhedral without reaction rims or signs of resorption, suggesting they were liquidus phases, with their host magmas erupting too rapidly for significant reequilibration. Olivine has a weak, negative correlation with SiO_2 (Figure 4f) and a weaker positive correlation with Mg number, the latter affected by the variable SiO_2–Mg number trends of the volcanic centers (Figure 4c).

[59] On the basis of extinction angle measurements, plagioclase compositions are typically in the labradorite range (An_{53-67}; mean An_{59}) for basalt–andesite and the andesine–labradorite range (An_{42-60}; mean An_{52}) for andesite–dacite–rhyolite. Compositions are consistently low in K_2O (<0.5%; typically <0.2%) and high in Fe_2O_3 (≤1.5%) [*Peckett*, 2006], as was observed previously for Kermadec arc tholeiites [*Brothers and Hawke*, 1981]. Many plagioclase phenocrysts (33% of samples) show resorption or have reaction rims of pyroxene±Fe-Ti oxides (Figure 8c) (38% of samples). These features, together with reverse zoning seen in some lavas (particularly Hinetapeka), reflect P–T fluctuations in the magma and/or mixing of magmas of contrasting composition or temperature. Monowai lavas rarely show such features, whereas in Hinepuia lavas they are common.

[60] Pyroxene compositions range from hypersthene (En_{48} to En_{67}), through pigeonite ($En_{44}Wo_{10}$ to $En_{41}Wo_9$) to diopside-augite ($En_{45}Wo_{47}$ to $En_{36}Wo_{28}$) [*Peckett*, 2006]. Resorption and reaction rims are relatively common (e.g., Figure 8d), except in Monowai and (curiously) Hinepuia lavas. Orthopyroxenes typically have reaction rims of

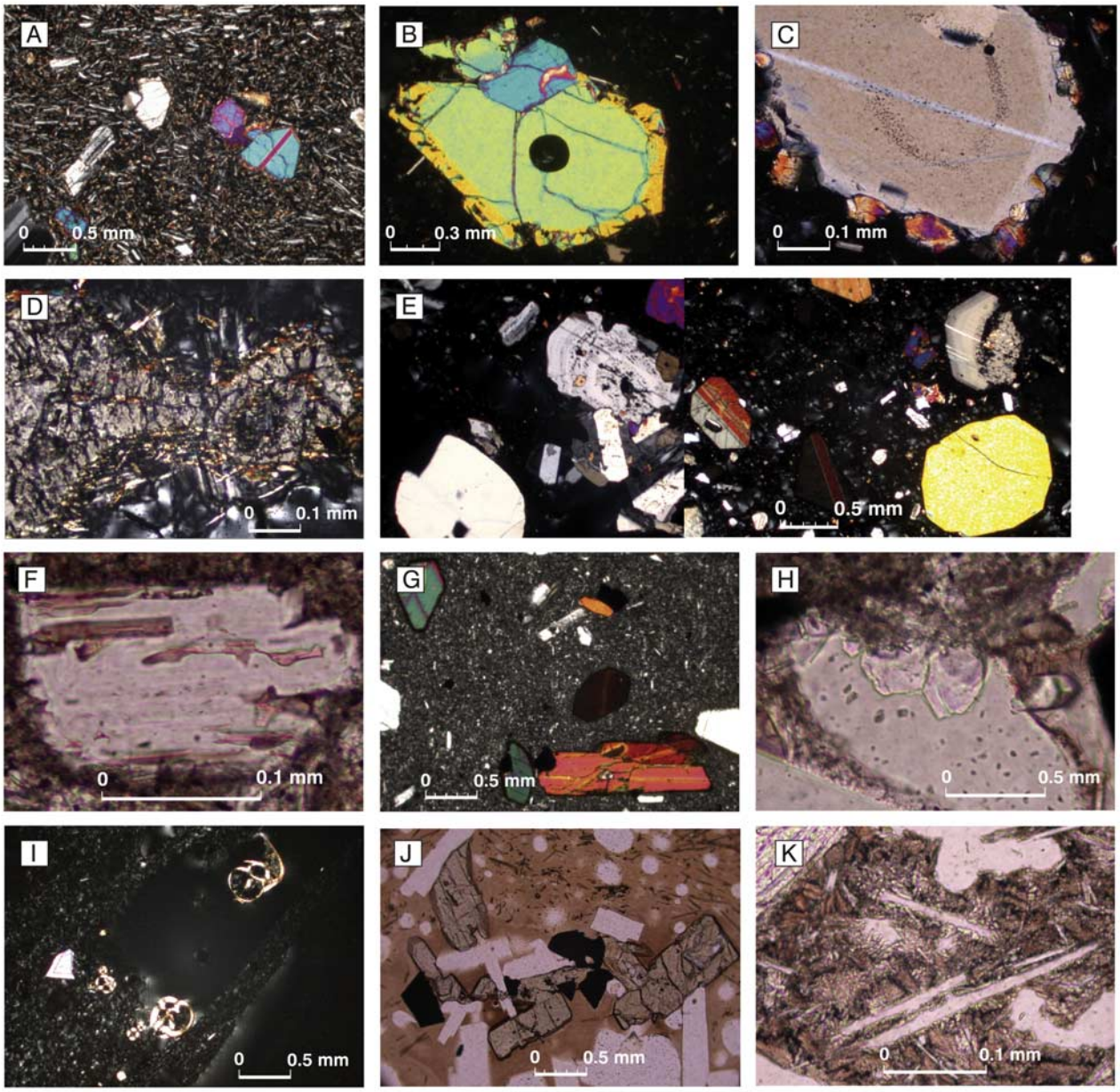

Figure 8. Photomicrographs of NKST lavas: (a) Plagioclase, pyroxene and olivine phenocrysts in an intergranular matrix of plagioclase laths, pyroxene and Fe-Ti oxides, in andesite from Putoto (PuC1; P72483; crossed polarized light). (b) Disequilibrium olivine in andesite from Hinetapeka (HtC2; P72498; crossed polarized light). (c) Plagioclase phenocryst with a reaction rim of pyroxene, in basalt from Putoto (PuP5; P72467; crossed polarized light). (d) Resorbed clinopyroxene phenocryst with a reaction rim of orthopyroxene, plagioclase and Fe-Ti oxide, in dacite from Rakahore (RkC2; P72428; crossed polarized light). (e) Coexisting unreacted quartz (left) and olivine (right) with sieved plagioclase, in rhyolite from Hinepuia (HpV; P72356; crossed polarized light—two images from the same thin-section). (f) Sieved plagioclase in dacite from Hinetapeka (HtC2; P72498; plane light. (g) Hornblende, Fe-Ti oxides, plagioclase and felsitic matrix, in rhyolite from Hinepuia (HpC2; P72403; crossed-polarized light). (h) Equant cristobalite and tridymite crystals with acicular pyroxene protruding into a vesicle (GaV; P72462; plane light). (i) Benthic foraminifera trapped in vesicle glass (RkC2; P72428, crossed polarized light). (j) Quench crystallites in glassy groundmass, increasing toward the flow rim (MoC2; P72220; plane light). (k) Quenched plumose pyroxenes and swallow-tailed plagioclase in glassy matrix (MoV; P72284; plane light).

clinopyroxene ± plagioclase, particularly in lavas from Hinetapeka, Putoto, and "V."

[61] Accessory minerals, including Fe-Ti oxides, silica polymorphs, apatite, and alkali-feldspar, occur in varying proportions in the lavas depending on bulk-rock composition and the proportion of residual melt (glass). Fe-Ti oxides are ubiquitous, ranging between 19% in a Putoto basaltic andesite and 0.1% in a Monowai basalt. The Fe-Ti oxides occur typically as fine crystals disseminated through the groundmass, but in Monowai and "V" lavas, dendritic habit is common. Despite being strongly quartz-normative, just 38% of andesites–dacites–rhyolites contain quartz phenocrysts, with the Hinepuia rhyolite (7–9%) being the only lava with more than 3%. Other evolved lavas have quench tridymite–cristobalite in their groundmasses (e.g., 17% in P72502), but the relative rarity of these silica polymorphs (and alkali feldspar) reflects the high glass contents. Apatite is common in andesites–dacites–rhyolites (47% of samples) but rarer in basalts–andesites (15%). Zircon was not observed.

7.3.2. Disequilibrium Assemblages and Textures

[62] Disequilibrium assemblages and reaction overgrowths on olivine (e.g., Figure 8b), plagioclase (e.g., Figure 8c), and pyroxene (e.g., Figure 8d) indicate compositional readjustment during ascent [*Shelley*, 1993], and in some cases, magma mingling or mixing in high-level magma reservoirs. Magma mingling is most strongly evident in andesites–dacites from Hinepuia, which show macroscopic evidence for blending of basaltic or andesitic and rhyolitic magma and unusually elevated Mg numbers (Figure 4c). The mingled magmas contain unreacted quartz and forsteritic olivine (Figure 8e), bimodal plagioclase compositions of An_{49} and An_{75}, Mg-rich orthopyroxene of En_{60}, and ilmenite with titanomagnetite of basaltic affinity. Some silicic lavas from Hinetapeka, Gamble, Rakahore, and "U" exhibit similar features. Other evidence for complex magmatic histories includes the widespread occurrence of phenocrysts with resorbed margins and/or sieved interiors. The latter, resulting from the heating of phenocrysts above their liquidus, are abundant in plagioclase (Figure 8f) but less so in pyroxene. Such features are frequently attributed to magma mixing [*Tsuchiyama*, 1985], but similar textures can be produced by decompression during magma ascent, due to rapid undercooling resulting from volatile release [*Pearce et al.*, 1987; *Kuo and Kirkpatrick*, 1982]. Thus, hornblende typically reacts out, and its rare occurrence in the Hinepuia rhyolite (Figure 8g) is due to very rapid ascent, with only a thin reaction rim formed. Sieve textures in plagioclase are ubiquitous in Hinetapeka, Putoto, Hinepuia and "U" lavas, relatively common in "V" lavas, and rare in Monowai lavas.

[63] Xenoliths are uncommon in basalts–andesites but are more frequent (38% of samples) in andesites–dacites–rhyolites, their abundance negatively correlated with phenocryst content. Most xenoliths are basaltic, andesitic, or microdioritic, although dacitic–rhyolitic compositions occur in three lavas. Xenoliths are particularly common in the Hinepuia mixed magmas, consistent with rapid ascent and erosion of the conduit walls. Restitic material is not recognized in any of the lavas. The apparent paucity of xenoliths in the more basic lavas may be a question of identification; cognate mineral aggregates are difficult to distinguish from glomerocrysts, which occur in most samples and often in high abundance. Similarly, embayed xenocrysts with clear reaction rims are easily distinguished, but some "phenocrysts" may be nontextured xenocrysts.

7.3.3. Degassing and Quench Textures

[64] Nearly all recovered lavas are weakly to strongly vesicular. Given the sampling bias toward young scoria cones and pumiceous domes (Table 2), this is to be expected. Vesicles range from gas blisters 50 cm or more in diameter (Figure 3h) to angular voids between microphenocrysts. Such diktytaxitic voids occasionally coalesce to produce drusy vesicles lined with needles of pyroxene, plagioclase or cristobalite-tridymite (Figure 8h). These features are particularly common in basalts–andesites erupted from Monowai and "V." Other vesicles have glassy linings, sometimes with foraminifera trapped within (Figure 8i), or are recrystallized to Fe-Ti oxides, cristobalite, or tridymite. Elongated vesicles indicating magma flow occur in some andesites from Hinetapeka (e.g., Figure 3a), Putoto, Monowai, and "V." Stretching is particularly common in Hinepuia andesites–dacites and Rakahore dacites–rhyolites, where a woody texture is imparted to the rocks (e.g., Figure 3d).

[65] Many of the basalts–andesites are scoriaceous, containing on average 24% and as much as 57% vesicles (Table 6). Andesites–dacites–rhyolites are typically more vesicular (mean 33%) reflecting higher primary volatile contents, with some pumiceous dacites and rhyolites having >60% vesicles. The absence of a strong negative correlation between vesicle content and LOI suggests that most degassing occurred at depth as a result of crystallization and depressurization. LOI is, however, correlated with total glass content (Figure 4e), particularly for the more silicic rocks, indicating that residual volatiles remained trapped in the glass after eruption. Positive correlations between LOI and silica content for many of the basalts–andesites, particularly those from Monowai (Figure 4d), could be explained by increasing amounts of residual, volatile-rich fluid during fractional crystallization. The lack of such correlations for most of the andesites–dacites–rhyolites suggests that a different process may be at work (crustal anatexis).

[66] Mean phenocryst contents are almost constant across the full compositional range (14–18%; Table 6), but andesites–dacites–rhyolites have nearly four times the average glass content of the basalts–andesites, up to 97% in a high-silica dacite from Rakahore. Quench textures in microphenocrysts or groundmass microlites are widespread, resulting from rapid cooling in cold seawater. The occurrence and styles of quench textures, together with observations of dredged volcanic material and undersea photographs (only a few are available; see Figure 3g) give an indication of the eruption mechanisms operating. In the southern Kermadec arc (SKA; Figure 1a), basaltic–andesitic edifices show a general transition from effusive pillow lavas, massive sheet flows and talus breccias below 700–1000 mbsl to fragmental and scoriaceous hyaloclastite to pyroclastic deposits above [*Wright*, 1996; *Wright et al.*, 2002; *Wright et al.*, 2003]. Sampling at relatively shallow depth in the NKST arc is thus consistent with the recovery of mainly pyroclastic and fragmental material but, in the absence of extensive seafloor photography, this cannot be quantified.

[67] Quenching relates to different degrees of undercooling, with high degrees of undercooling resulting in melt

retention in the form of glass. This is particularly so for pumiceous rocks generated by explosive submarine eruption. It is notable that the laminated rhyolites from Gamble have much lower glass contents (35–61%) than their pumiceous counterparts (79–97%). Hinepuia rhyolite is unusual, with no glass, hornblende phenocrysts and very low volatile contents (~0.2 wt%; Figure 4d). Its felsitic texture (Figure 8g) may have resulted from sudden undercooling induced by rapid devolatilization [*Swanson et al.*, 1989]. Some of the Monowai basalts are particularly glass-rich (≤41%), indicating very rapid quenching, but most sampled basalts have <10% glass, as is more typical of basaltic magmas globally [*Shelley*, 1993].

[68] Slightly lower degrees of quenching result in hyalopilitic or intersertal textures and the generation of fine-grained, indeterminate crystallites (Figure 8j), microlites of tridymite and cristobalite, plumose, feathery or sheaf-like pyroxene, plumose or swallow-tailed plagioclase (Figure 8k), disseminated or dendritic Fe-Ti oxides and skeletal forms. Starburst, whisker, spherulitic, plumose, or sheave-like crystal forms are prevalent in the explosively ejected scoria or pillow lavas from Monowai and "V," whereas the extrusive lavas from "U" show relatively few quench textures of any type.

[69] Other crystal growth forms such as ophitic or poikilitic textures are not uncommon and, like resorption and sieving, reflect compositional and/or P–T changes in the melt during ascent. The more viscous silicic rocks, in which high degrees of melt polymerization inhibits nucleation, tend to have higher glass contents, particularly pumiceous varieties quenched rapidly. Phenocryst-rich, laminated varieties (e.g., P92456; Figure 3b) have textures resulting from slower crystal growth in slightly undercooled magma that has extruded rather than erupted explosively. In these lavas, crystallites are widespread and swallow-tailed microlites occur. There is strong evidence that the mingled Hinepuia dacites were explosively erupted. In addition to being pumiceous, with high glass contents, many of the rocks contain skeletal or needle-like plagioclase microlites, and often contain fractured and strained plagioclase and pyroxene phenocrysts, produced by abrasion and shearing during eruption.

8. Conclusions

[70] On the basis of multibeam mapping and seafloor sampling we make the following observations and deductions regarding the NKST arc segment:

[71] 1. The segment comprises at least seven volcanic centers and includes Monowai, now recognized as a complex stratovolcano–multiple caldera system.

[72] 2. All NKST volcanic centers are on, or immediately to west of, the Kermadec Ridge crest and all contain calderas, multiple parasitic cones, domes, fissure ridges, and vent fields.

[73] 3. Within centers, there are strong structural controls on edifice location, with cones and fissure ridges associated with faulting parallel to or perpendicular to the regional northeast–southwest trend of the arc–trench system. Ring faults mark the margins of the calderas, many of which are northwest–southeast orientated, in the direction of least compressive stress.

[74] 4. Recovered lavas are low-K tholeiites ranging from basalt to rhyolite, with two centers yielding only dacites–rhyolites (i.e., >69% SiO_2) and two others only basalts–andesites (i.e., <63% SiO_2). Dacite is the most common rock type, but the overall volume-weighted mean composition is andesite (~62% SiO_2).

[75] 5. Recovered lavas are highly vesicular and glassy and contain quench textures indicating degassing at depth and rapid cooling after mainly pyroclastic eruption. Effusive eruptives are rare, due to the relatively shallow depth of eruption (<1000 mbsl).

[76] 6. Disequilibrium textures, including sieved phenocrysts, reaction overgrowths, melt and mineral inclusions, xenocrysts and xenoliths, suggest complex magmatic histories involving fractional crystallization, magma mixing, and crustal assimilation/anatexis. This is particularly so for lavas from Hinepuia, which show strong evidence for magma mixing immediately prior to eruption. Monowai lavas, in contrast, show few signs of disequilibrium and may have been erupted rapidly from deeper reservoirs. The exclusively silicic Gamble and Rakahore lavas may be crustal melts, but the presence of andesitic xenoliths and olivine xenocrysts suggests that mafic magmas were involved in their genesis.

[77] 7. Silicic lava (at least for the recent eruptives) is a major component of the NKST arc sector and caldera-formation is the dominant eruptive style. The scale and longitudinal extent of silicic magmatism from south of the Kermadec Islands to the southern Tofua Arc, where the volcanic front lies near the ridge crest, is in marked contrast to basaltic-andesitic stratovolcano formation to the south. With evidence from other arcs, silicic magma is now recognized as a major component of intraoceanic arc volcanism globally.

Appendix A: Volcanic Rocks Dredged From the NKST Sector

[78] This compilation contains XRF analyses of all recovered samples assessed to contain less than 5% alteration minerals; those with more than 5% alteration minerals ("Alteration") + xenoliths ('Xenoliths') are not included in major element plots (Figure 4) or in mean weighted composition calculations.

[79] For major element analysis, dried powder was mixed with lithium tetraborate and ammonium nitrate, fused to a homogeneous glass bead and analyzed on a Philips 1400 spectrometer, calibrated against GSJ rock standards JB-2, JA-1, and JR-1. Loss on ignition (LOI) was determined by weight loss of 3 g of powder heated to 1000°C for 4 h in a silica crucible.

[80] Compiled analyses are normalized to 100%, volatile-free, with total iron adjusted to the following FeO/Fe_2O_3 ratios: basalt, 0.20; basaltic andesite, 0.30; andesite, 0.35; dacite, 0.4, rhyolite, 0.50. "Total*" is the original measured total. Multiple analyses of samples of the same lava are averaged and treated as single analyses to reduce duplication bias (such analyses are indicated by multiple field numbers, with samples assessed petrographically emboldened).

[81] In calculating compositional weightings, each dredging is taken to represent the lithological makeup of a sampling site. Sample weightings ("S-weightings") are

Table A1.

Field Number	**P72498**	**P72503**	P72494 **P72499**	**P72502** P72504	**P72495**	P72511 **P72512**	**P72505** **P72506**	**P72490** **P72491**	**P72476** **P72478**	**P72480**	**P72483**	**P72492**	**P72479**	**P72475**
Center	Hinetapeka	Hinetapeka	Hinetapeka	Hinetapeka	Hinetapeka	Hinetapeka	Hinetapeka	Putoto	Putoto	Putoto	Putoto	Putoto	Putoto	Putoto
Edifice	HtC2	HtC2 (HtR1)	HtC2	HtC2 (HtR1)	HtC2	HtC3 (HtR2)	HtC3 (HtR2)	PuC1	PuC1	PuC1	PuC1	PuR1	PuC1	PuC1
Volume	0.983	0.983	0.983	0.983	0.983	0.017	0.017	0.394	0.394	0.394	0.394	0.394	0.394	0.394
Samples	4	1	5	2	3	1	1	2	6	2	2	2	2	3
S-weighting	0.200	0.050	-	0.100	0.150	0.250	0.250	0.053	0.158	0.053	0.053	0.053	0.053	0.079
V-weighting	0.393	0.098	-	0.197	0.295	0.008	0.008	0.054	0.161	0.054	0.054	0.054	0.054	0.081
Alteration	4%	<1%	<1%	≪1%	0%	3%	<1%	<1%	1%	≪1%	2%	2%	1%	5%
Xenoliths	0%	0%	20%	0%	0%	0%	0%	0%	0%	0%	0%	2%	0%	0%
SiO_2	59.67	65.06	67.03	66.99	68.18	55.98	61.45	50.37	53.80	55.39	57.57	60.20	65.22	65.39
TiO_2	0.78	0.69	0.65	0.62	0.56	0.98	0.96	0.74	0.93	0.76	0.77	0.89	0.68	0.59
Al_2O_3	15.32	14.63	14.33	14.33	15.12	15.68	14.26	18.95	15.38	14.26	15.63	14.87	14.29	14.00
Fe_2O_3	2.42	2.14	1.73	1.88	1.38	2.63	2.61	1.71	2.73	2.21	2.36	2.70	2.41	2.51
FeO	6.92	5.35	4.33	4.70	3.45	8.77	7.45	8.56	9.08	7.36	6.74	7.73	6.03	6.28
MnO	0.20	0.16	0.17	0.15	0.14	0.20	0.20	0.18	0.21	0.17	0.18	0.22	0.20	0.21
MgO	3.32	1.74	1.72	1.46	1.33	3.52	2.14	5.13	4.88	6.33	4.31	2.30	1.16	1.04
CaO	7.58	5.76	5.09	5.16	4.87	8.86	6.53	12.09	9.85	10.35	8.90	6.74	4.99	4.95
Na_2O	3.10	3.61	4.01	3.81	4.05	2.79	3.50	2.02	2.58	2.66	2.97	3.72	4.21	4.20
K_2O	0.54	0.74	0.79	0.79	0.79	0.46	0.74	0.19	0.44	0.39	0.41	0.50	0.63	0.64
P_2O_5	0.16	0.13	0.15	0.13	0.14	0.12	0.17	0.07	0.11	0.11	0.16	0.14	0.19	0.19
LOI	1.42	0.86	2.52	0.90	0.60	0.63	0.97	0.45	0.64	0.39	0.74	1.04	0.16	0.75
Total*	100.30	99.92	101.78	100.12	100.03	99.28	100.12	99.49	99.51	99.31	99.99	99.62	99.39	99.74

Field Number	**P72467**	**P72473**	**P72460**	P72456 **P72461** P72463	**P72448** P72449	P72455 **P72462**	**P72454**	**P72447**	**P72423**	**P72434**	**P72422**	**P72435**	**P72428** P72429	**P72442** P72443	**P72388**	**P72393**
Center	Putoto	Putoto	Gamble	Gamble	Gamble	Gamble	Gamble	Gamble	Rakahore	Rakahore	Rakahore	Rakahore	Rakahore	Rakahore	Hinepuia	Hinepuia
Edifice	PuC2 (PuP5)	PuC2 (PuP5)	GaV	GaV	GaV	GaV	GaV	GaV	RkC1 (RkR1)	RkC1	RkC1 (RkR1)	RkC1	RkC2	RkP2	HpC2 (HpP2)	HpC2 (HpP2)
Volume	0.377	0.377	1.000	1.000	1.000	1.000	1000	1.000	0.799	0.799	0.799	0.799	0.201	0.201	0.040	0.040
Samples	6	2	1	7	6	2	2	1	1	5	5	3	2	5	1	1
S-weighting	0.375	0.125	-	0.438	0.375	0.125	-	0.063	-	0.192	0.192	0.115	0.500	-	0.017	0.017
V-weighting	0.367	0.122	-	1.000	1.000	1.000	-	1.000	-	0.307	0.307	0.183	0.201	-	0.001	0.001
Alteration	0%	2%	0.5%	0%	0%	≪1%	0%	2	1%	1%	≪≪1%	0%	3%	3%	0%	≪1%
Xenoliths	0%	0%	5%	0%	0%	0%	10%	0%	15%	0%	0%	0%	0%	5%	0%	2%
SiO_2	50.34	52.04	72.44	72.94	73.18	73.32	74.12	74.38	71.30	71.48	72.42	72.52	69.42	72.35	49.83	59.71
TiO_2	0.52	0.70	0.50	0.48	0.47	0.46	0.42	0.39	0.49	0.48	0.46	0.46	0.55	0.46	0.46	0.43
Al_2O_3	18.19	15.86	13.70	13.58	13.52	13.56	13.42	13.18	14.58	14.46	14.18	14.14	14.12	14.20	18.62	15.21
Fe_2O_3	1.59	2.68	1.20	1.15	1.13	1.09	0.96	1.01	0.95	0.95	1.01	1.02	1.37	1.02	1.41	1.76
FeO	7.94	8.92	2.39	2.30	2.25	2.18	1.93	2.02	2.37	2.38	2.02	2.04	3.41	2.04	7.07	5.03
MnO	0.18	0.22	0.17	0.16	0.16	0.16	0.15	0.15	0.11	0.11	0.10	0.10	0.19	0.10	0.15	0.13
MgO	6.27	5.96	0.78	0.65	0.60	0.58	0.49	0.46	0.81	0.81	0.71	0.68	1.23	0.70	7.29	5.84
CaO	13.28	11.61	3.29	3.19	3.13	3.08	2.94	2.81	4.00	3.93	3.64	3.57	4.51	3.65	13.66	8.85
Na_2O	1.52	1.79	4.74	4.74	4.73	4.77	4.71	4.72	4.45	4.41	4.47	4.48	4.43	4.49	1.32	2.44
K_2O	0.13	0.17	0.68	0.71	0.74	0.71	0.78	0.80	0.82	0.86	0.88	0.86	0.63	0.86	0.14	0.56
P_2O_5	0.04	0.05	0.12	0.11	0.10	0.10	0.09	0.08	0.12	0.12	0.10	0.11	0.15	0.11	0.04	0.06
LOI	0.49	0.39	0.51	0.74	1.18	0.37	2.61	1.14	1.44	1.20	1.83	1.55	1.09	1.37	0.51	0.55
Total*	99.23	99.04	100.16	99.94	100.44	99.58	102.1	100.42	100.91	100.55	101.32	101.20	100.04	100.73	99.38	99.40

Table A1. (continued)

Field Number	**P72402**	**P72391** P72392	**P72416** P72418	**P72401**	**P72389**	**P72400**	**P7230**	**P72404** P72405	**P72403**	**P72356**	**P72360**	**P72366**	**P72358**	**P72239**	**P72236**–38 P72340
Center	Hinepuia	Hinepuia	Hinepuia	Hinepuia	Hinepuia	Hinepuia	Hinepuia	Hinepuia	Hinepuia	Hinepuia	Hinepuia	Hinepuia	Hinepuia	Monowai	Monowai
Edifice	HpC2	HpC2 (HpP2)	HpC2 (HpP1)	HpC2	HpC2 (HpP2)	HpC2	HpC2 (HpP2)	HpC2	HpC2	HpV	HpV	HpV	HpV	MoC1	MoC1
Volume	0.040	0.040	0.040	0.040	0.040	0.040	0.040	0.040	0.040	0.960	0.960	0.960	0.960	0.469	0.469
Samples	3	6	5	1	1	2	3	5	2	4	1	2	2	3	7
S-weighting	0.050	0.100	0.083	0.017	-	0.033	0.050	0.100	0.033	0.222	0.056	0.111	0.111	0.048	0.111
V-weighting	0.004	0.008	0.007	0.001	-	0.003	0.004	0.008	0.003	0.427	0.107	0.213	0.213	0.067	0.156
Alteration	<1%	4%	0%	<1%	0%	<1%	2%	≪1%	0%	≪1%	0%	≪1%	<1%	≪≪1%	0%
Xenoliths	2%	0%	0%	2%	9%	0%	0%	0%	1%	1%	1.5%	0%	4%	0%	0%
SiO_2	62.58	66.06	66.25	66.42	67.10	67.30	67.53	72.53	72.94	61.12	64.65	66.04	67.04	51.67	52.33
TiO_2	0.44	0.46	0.46	0.46	0.44	0.43	0.44	0.37	0.37	0.44	0.46	0.46	0.45	0.67	0.75
Al_2O_3	15.17	15.08	15.08	15.02	15.06	14.91	14.78	14.08	13.84	15.27	15.28	15.12	14.93	15.96	15.41
Fe_2O_3	1.62	1.61	1.60	1.58	1.46	1.46	1.48	1.00	1.01	1.69	1.63	1.53	1.48	1.83	2.57
FeO	4.62	4.02	3.99	3.96	3.66	3.66	3.69	2.00	2.03	4.84	4.06	3.82	3.70	9.16	8.56
MnO	0.12	0.11	0.11	0.11	0.11	0.11	0.11	0.08	0.08	0.13	0.11	0.11	0.11	0.22	0.21
MgO	4.24	2.35	2.28	2.25	2.15	2.09	2.06	0.88	0.88	4.86	3.24	3.08	2.30	6.25	6.25
CaO	7.63	6.13	5.99	5.94	5.74	5.64	5.52	3.67	3.54	8.34	6.61	5.60	5.70	11.92	11.50
Na_2O	2.85	3.28	3.31	3.33	3.38	3.41	3.42	4.18	4.11	2.63	3.10	3.33	3.37	2.06	2.13
K_2O	0.68	0.83	0.86	0.87	0.83	0.91	0.91	1.12	1.13	0.62	0.79	0.83	0.84	0.19	0.22
P_2O_5	0.06	0.07	0.06	0.06	0.07	0.06	0.06	0.07	0.07	0.06	0.07	0.07	0.07	0.06	0.07
LOI	0.60	1.01	1.21	1.22	1.04	1.33	1.20	0.20	0.20	1.11	1.05	1.06	1.70	0.66	0.69
Total*	99.79	100.18	100.31	100.38	100.59	100.66	100.43	99.40	99.59	100.27	100.25	100.20	100.92	99.01	99.49

Field Number	**P72328** P72329	**P72248**	**P72223**	**P72224**	**P72222**	**P72220**	**P72269**	P72261, 72, **84** 87, 88	**P22996**	**P72258**	**P72295**	**P72260**	P72299–02 P72316, **19**	**P72257**
Center	Monowai	Monowai	Monowai	Monowai	Monowai	Monowai	Monowai	Monowai	Monowai	Monowai	Monowai	Monowai	Monowai	Monowai
Edifice	MoC1 (MoP3)	MoC2 (MoR1)	MoC2	MoC2	MoC2	MoC2	MoV	MoV	MoV	MoV	MoV	MoV	MoV	MoV
Volume	0.469	0.180	0.180	0.180	0.180	0.180	0.329	0.329	0.329	0.329	0.329	0.329	0.329	0.329
Samples	11	2	6	1	7	2	3	28	3	5	1	1	29	1
S-weighting	0.175	0.037	0.111	0.019	0.130	0.037	0.014	0.131	0.014	0.023	0.005	0.005	0.136	0.005
V-weighting	0.246	0.020	0.060	0.010	0.070	0.020	0.015	0.138	0.015	0.025	0.005	0.005	0.143	0.005
Alteration	<1%	≪≪1%	≪≪1%	≪≪1%	3%	<1%	0%	≪1%	0%	0%	≪1%	1%	0%	≪1%
Xenoliths	0%	0%	0%	0%	0%	0%	2%	0%	0%	0%	0%	0%	0%	0%
SiO_2	53.71	51.77	56.94	57.63	58.26	62.87	49.15	49.33	49.63	49.74	50.04	50.23	50.46	50.61
TiO_2	1.18	0.68	1.07	1.01	1.12	0.95	0.43	0.45	0.48	0.49	0.52	0.54	0.56	0.58
Al_2O_3	14.50	15.89	14.83	15.15	14.91	13.48	19.25	18.77	18.01	17.54	16.86	16.39	16.00	15.57
Fe_2O_3	3.06	1.84	3.02	2.81	2.83	2.74	1.44	1.47	1.55	1.59	1.65	1.70	1.77	1.79
FeO	10.21	9.21	8.62	8.02	8.07	7.82	7.19	7.37	7.76	7.95	8.27	8.52	8.83	8.94
MnO	0.23	0.22	0.22	0.21	0.21	0.22	0.17	0.17	0.18	0.19	0.19	0.20	0.21	0.21
MgO	4.54	6.26	3.40	3.15	3.05	1.30	6.63	6.75	6.85	7.12	7.19	7.28	7.15	7.34
CaO	9.40	11.83	7.91	7.89	7.51	5.35	41.03	13.94	13.70	13.54	13.38	13.14	13.11	13.02
Na_2O	2.73	2.05	3.30	3.42	3.34	4.19	1.50	1.55	1.62	1.62	1.66	1.81	1.71	1.71
K_2O	0.33	0.20	0.52	0.54	0.55	0.84	0.16	0.16	0.17	0.17	0.18	0.14	0.18	0.17
P_2O_5	0.12	0.06	0.15	0.16	0.16	0.24	0.04	0.04	0.05	0.05	0.05	0.05	0.05	0.05
LOI	0.74	0.92	0.91	1.27	1.53	1.66	0.38	0.40	0.39	0.39	0.43	0.53	0.58	0.59
Total*	98.99	99.52	99.71	99.93	100.13	100.98	99.29	99.22	98.98	99.37	99.24	99.30	99.38	99.39

Table A1. (continued)

Field	P72339	P72347	P72341	P72346	P72340	P72350	P72203	P72206	P72205	P72176	P72178	P72187
Number	P72342					P72352	P72204			P72177		P72190
Center	'U'	'U'	'U'	'U'	'U'	'U'	'V'	'V'	'V'	'V'	'V'	'V'
Edifice	UC1	UC1	UC1	UC1	UC1	UC1	VP1	VP1	VP1	VC2 (VP2)	VC2 (VP2)	VC2
Volume	1.000	1.000	1.000	1.000	1.000	1.000	0.171	0.171	0.171	0.879	0.879	0.879
Samples	3	1	1	1	-	2	11	1	4	8	1	3
S-weighting	0.375	0.125	0.125	0.125	-	0.250	0.344	0.031	0.125	0.333	0.042	0.125
V-weighting	1.000	1.000	1.000	1.000	-	1.000	0.083	0.008	0.030	0.586	0.073	0.220
Alteration	0%	0%	<1%	<1%	3%	1%	≪1%	0%	≪1%	≪1%	1%	1%
Xenoliths	0%	0%	2%	2%	8%	1%	0%	0%	0%	0%	0%	0%
SiO_2	51.42	52.10	63.07	66.51	68.02	71.29	49.69	49.83	50.23	54.17	56.57	61.75
TiO_2	1.04	0.96	0.76	0.65	0.70	0.54	0.76	0.81	0.87	0.96	1.04	0.84
Al_2O_3	15.52	17.77	15.48	15.10	14.52	13.90	18.55	18.42	17.51	15.44	14.44	14.46
Fe_2O_3	2.23	2.53	2.03	1.68	1.57	1.39	1.81	1.87	1.96	2.90	2.90	2.62
FeO	11.15	8.44	5.08	4.20	3.93	2.78	9.04	9.34	9.78	9.66	9.66	7.50
MnO	0.25	0.20	0.17	0.17	0.17	0.15	0.19	0.20	0.21	0.23	0.23	0.23
MgO	5.21	4.15	2.25	1.34	1.13	0.69	5.34	5.01	5.17	4.24	3.43	2.05
CaO	10.44	10.87	6.36	5.11	4.27	3.37	12.60	12.42	12.06	9.62	8.42	6.70
Na_2O	2.29	2.48	3.82	4.26	4.57	4.83	1.79	1.87	1.97	2.46	2.88	3.39
K_2O	0.34	0.37	0.78	0.79	0.90	0.92	0.16	0.17	0.17	0.23	0.29	0.34
P_2O_5	0.10	0.12	0.20	0.19	0.22	0.12	0.06	0.07	0.07	0.10	0.12	0.12
LOI	0.67	0.45	0.41	0.38	0.86	0.48	0.65	0.69	0.76	0.61	0.82	1.29
Total*	99.06	99.29	99.68	99.49	100.37	99.77	99.35	99.40	99.18	99.10	99.45	100.42

the relative proportions of different lithologies from an edifice weighted according the number of samples of closely similar composition (“Samples”), as determined by chemical analysis and/or visual inspection, assuming all sampling sites are of equal importance. Volume weightings (“V-weightings”) are sample weightings adjusted to the proportional constructional volumes (“Volume”) of the sampled edifices within a center.

[82] **Acknowledgments.** We thank the captain and crew of R/V *Tangaroa* and the coleaders and other scientific members of the NZAPLUME III expedition for their support and assistance during mapping and petrological sampling. Thanks also to Arne Pellentin (NIWA) for producing the multibeam maps and for undertaking the volume calculations and to John Gamble of Cork University (Ireland) for helpful advice. Suzannah Toulmin, Andrew Gray, and Carolyn Hume (GNS Science) created the graphics, and Philip Warnes (GNS Science) took the hand specimen photographs. This research was funded by the New Zealand Foundation for Research, Science and Technology contracts C05X0406 and C01X0702.

References

Acocella, V., T. Korme, F. Salvini, and R. Funiciello (2002), Elliptic calderas in the Ethiopian Rift: Control of pre-existing structures, *J. Volcanol. Geotherm. Res.*, *119*, 189–203, doi:10.1016/S0377-0273(02)00342-6.

Baker, E. T., R. A. Feely, C. E. J. de Ronde, G. J. Massoth, and I. C. Wright (2003), Submarine hydrothermal venting on the southern Kermadec volcanic arc front (offshore New Zealand): Location and extent of particle plume signatures, in *Intra-Oceanic Subduction Systems: Tectonic and Magmatic Processes*, edited by R. D. Larter and P. T. Leat, *Geol. Soc. London Spec. Publ.*, *219*, 141–161.

Brothers, R. N., and M. M. Hawke (1981), The tholeiitic Kermadec volcanic suite: Additional field and petrological data including iron-enriched plagioclase feldspars, *N. Z. J. Geol. Geophys.*, *24*, 167–175.

Campbell, M. E., J. Rowland, I. C. Wright, and I. E. M. Smith (2007), Oblique rifting along the central and southern Kermadec arc front (30°–36°S), SW Pacific, *Geochem. Geophys. Geosyst.*, *8*, Q01007, doi:10.1029/2006GC001504.

Crawford, A. J., T. J. Falloon, and S. Eggins (1987), The origin of island arc high-alumina basalts, *Contrib. Mineral. Petrol.*, *97*, 417–430, doi:10.1007/BF00372004.

Crawford, W. C., J. A. Hildebrand, L. M. Dorman, S. C. Webb, and D. A. Wiens (2003), Tonga Ridge and Lau Basin crustal structure from seismic refraction data, *J. Geophys. Res.*, *108*(B4), 2195, doi:10.1029/2001JB001435.

Davey, F. J. (1980), The Monowai Seamount: An active submarine volcanic center on the Tonga-Kermadec ridge, *N.Z. J. Geol. Geophys.*, *23*, 533–536.

Delteil, J., E. Ruellan, I. C. Wright, and T. Matsumoto (2002), Structure and structural development of the Havre Trough (SW Pacific), *J. Geophys. Res.*, *107*(B7), 2143, doi:10.1029/2001JB000494.

DeMets, C., R. G. Gordon, D. F. Argus, and S. Stein (1994), Effect of recent revisions to the geomagnetic reversal time scale and estimates of current plate motions, *Geophys. Res. Lett.*, *21*(20), 2191–2194, doi:10.1029/94GL02118.

de Ronde, C. E. J., E. T. Baker, G. J. Massoth, J. E. Lupton, I. C. Wright, R. A. Feeley, and R. R. Greene (2001), Intra-oceanic subduction-related hydrothermal venting, Kermadec volcanic arc, New Zealand, *Earth Planet. Sci. Lett.*, *193*, 359–369, doi:10.1016/S0012-821X(01)00534-9.

de Ronde, C. E. J., K. Faure, C. J. Bray, D. A. Chappel, and I. C. Wright (2003), Hydrothermal fluids associated with seafloor mineralisation at two southern Kermadec arc volcanoes, offshore New Zealand, *Mineral. Deposita*, *38*, 217–233.

de Ronde, C. E. J., et al. (2005), Evolution of a submarine magmatic-hydrothermal system: Brothers volcano, southern Kermadec arc, New Zealand, *Econ. Geol.*, *100*, 1097–1133, doi:10.2113/100.6.1097.

de Ronde, C. E. J., I. C. Wright, and shipboard participants (2006), NZAPLUME III New Zealand American PLUme Mapping Expedition, cruise report, GNS Science, Lower Hutt, New Zealand.

Embley, R. W., and shipboard participants (2006), New Zealand American Submarine Ring of Fire 2005-Kermadec arc submarine volcanoes, cruise report, R/V *Ka'imikai-o-Kanaloa* and *Pisces V,* NOAA, Silver Spring, Md.

Ewart, A., W. B. Bryan, B. W. Chappell, and R. L. Rudnick (1994), Regional Geochemistry of the Lau-Tonga arc and back arc systems, *Proc. Ocean Drill. Program Sci. Results*, *135*, 385–425.

Gamble, J. A., I. E. M. Smith, M. T. McCulloch, I. J. Graham, and B. P. Kokelaar (1993), The geochemistry and petrogenesis of basalts from the Taupo Volcanic Zone and Kermadec Island arc, SW Pacific, *J. Volcanol. Geotherm. Res.*, *54*, 265–290, doi:10.1016/0377-0273(93)90067-2.

Gamble, J. A., I. C. Wright, J. Woodhead, and M. T. McCulloch (1995), Arc and backarc geochemistry in the southern Kermadec arc-Ngatoro Basin and offshore Taupo Volcanic Zone, SW Pacific, in *Volcanism Associated with Extension at Consuming Plate Margins*, edited by J. L. Smellie, *Geol. Soc. London Spec. Publ.*, *81*, 193–212.

Gamble, J. A., R. H. K. Christie, I. C. Wright, and R. J. Wysoczanski (1997), Primitive K-rich magmas from Clark volcano, southern Kermadec arc: A paradox in the K-depth relationship, *Can. Mineral.*, *35*, 275–290.

Haase, K. M., T. J. Worthington, P. Stoffers, D. Garbe-Schönberg, and I. C. Wright (2002), Mantle dynamics, element recycling, and magma genesis beneath the Kermadec arc-havre Trough, *Geochem. Geophys. Geosyst.*, *3*(11), 1071, doi:10.1029/2002GC000335.

Holohan, E. P., V. R. Troll, T. R. Walter, S. Munn, S. McDonnell, and Z. K. Shipton (2004), Elliptical calderas in active tectonic settings: An experimental approach, *J. Volcanol. Geotherm. Res.*, *144*, 119–136, doi:10.1016/j.jvolgeores.2004.11.020.

Holohan, E. P., B. van Wyk de Vries, and V. R. Troll (2008), Analogue models of caldera collapse in strike slip tectonic regimes, *Bull. Volcanol.*, *70*, 773–796, doi:10.1007/s00445-007-0166-x.

Kodaira, S., T. Sato, N. Takahaski, S. Miura, Y. Tamura, Y. Tatsumi, and Y. Kaneda (2007), New Seismological constraints on growth of continental crust in the Izu-Bonin intra-oceanic arc, *Geology*, *35*, 1031–1034, doi:10.1130/G23901A.1.

Kuo, L.-C., and R. J. Kirkpatrick (1982), Pre-eruption history of phyric basalts from DSDP legs 45 and 46: Evidence from morphology and zonation patterns in plagioclase, *Contrib. Mineral. Petrol.*, *79*, 13–27, doi:10.1007/BF00376957.

Leat, P. T., J. L. Smellie, I. L. Miller, and R. D. Larter (2003), Magmatism in the South Sandwich arc, in *Intra-Oceanic Subduction Systems: Tectonic and Magmatic Processes*, edited by R. D. Larter and P. T. Leat, *Geol. Soc. London Spec. Publ.*, *219*, 285–313.

Leat, P. T., R. D. Larter, and I. L. Miller (2007), Silicic magmas of Protector Shoal, South Sandwich arc: Indicators of generation of primitive continental crust in an island arc, *Geol. Mag.*, *144*, 179–190, doi:10.1017/S0016756806002925.

Le Maitre, R. W. (Ed.) (1989), *A Classification of Igneous Rocks and Glossary of Terms*, 193 pp., Blackwell, Oxford, U.K.

Lipman, P. (1997), Subsidence of ash-flow calderas: Relation to caldera size and magma-chamber geometry, *Bull. Volcanol.*, *59*, 198–218, doi:10.1007/s004450050186.

Lloyd, E. F., S. Nathan, I. E. M. Smith, and R. B. Stewart (1996), Volcanic history of Macauley Island, Kermadec Ridge, New Zealand, *N. Z. J. Geol. Geophys.*, *39*, 295–308.

Parson, L. M., and I. C. Wright (1996), The Lau-Havre-Taupo backarc basin: A southward propagating, multistage, evolution from rifting to spreading, *Tectonophysics*, *263*, 1–22, doi:10.1016/S0040-1951(96)00029-7.

Parsons, T., G. A. Thompson, and R. P. Smith (1998), More than one way to stretch: A tectonic model for extension along a plume track of the Yellowstone hotspot and adjacent Basin and range Province, *Tectonics*, *17*, 221–234, doi:10.1029/98TC00463.

Pearce, J. A., P. E. Basker, P. K. Harvey, and I. Luff (1995), Geochemical evidence for subduction fluxes, mantle melting and fractional crystallization beneath the South Sandwich arc, *J. Petrol.*, *36*, 1073–1109.

Pearce, T. H., J. K. Russell, and I. Wolfson (1987), Laser-interference and Normarski interference imaging of zoning profiles in plagioclase phenocrysts from the May 18, 1980 eruption of Mount St. Helens, Washington, *Am. Mineral.*, *72*, 1131–1143.

Peck, D. L., T. L. Wright, and J. G. Moore (1966), Crystallisation of tholeiitic basalt in Alae lava lake, Hawaii, *Bull. Volcanol.*, *29*, 629–655, doi:10.1007/BF02597182.

Peckett, K. M. (2006), The geochemistry and structure of the northern Kermadec arc, M.Sc. thesis, 177 pp, Univ. of Auckland, New Zealand.

Pelletier, B., and R. Louat (1989), Seismotectonics and present-day relative plate motions in the Tonga-Lau and Kermadec-Havre region, *Tectonophysics*, *165*, 237–250, doi:10.1016/0040-1951(89)90049-8.

Reyes, A. G. (2008), Petrological analysis and evaluation of volcanic rocks from the Northern Kermadec arc, *Sci. Rep. 2008/16*, 87 pp., GNS Sci., Lower Hutt, New Zealand.

Reyners, M. (1989), New Zealand seismicity 1964–87: An interpretation, *N. Z. J. Geol. Geophys.*, *32*, 307–315.

Robin, C., J.-P. Eissen, and M. Monzier (1993), Giant tuff cone and 12-km wide associated caldera at Ambrym Volcano (Vanuatu, New Hebrides arc), *J. Volcanol. Geotherm. Res.*, *55*, 225–238, doi:10.1016/0377-0273(93)90039-T.

Rowland, J. V., and R. H. Sibson (2001), Extensional fault kinematics within the Taupo Volcanic Zone, New Zealand: Soft-linked segmentation of a continental rift system, *N. Z. J. Geol. Geophys.*, *44*, 271–283.

Ruellan, E., J. Delteil, I. C. Wright, and T. Matsumoto (2003), From rifting to active spreading in the Lau Basin-Havre Trough backarc system (SW Pacific): Locking/unlocking induced by seamount chain subduction, *Geochem. Geophys. Geosyst.*, *4*(5), 8909, doi:10.1029/2001GC000261.

Shelley, D. (1993), *Igneous and Metamorphic Rocks Under the Microscope*, 445 pp., Chapman and Hall, London.

Shor, G. G., H. K. Kirk, and H. W. Menard (1971), Crustal structure of the Melanesian area, *J. Geophys. Res.*, *76*, 2562–2586, doi:10.1029/JB076i011p02562.

Smith, I. E. M., and R. C. Price (2006), The Tonga-Kermadec arc and Havre-Lau backarc system: Their role in the development of tectonic and magmatic models for the western Pacific, *J. Volcanol. Geotherm. Res.*, *156*, 315–331, doi:10.1016/j.jvolgeores.2006.03.006.

Smith, I. E. M., R. B. Stewart, and R. C. Price (2003a), The petrology of a large intra-oceanic silicic eruption: The Sandy Bay Tephra, Kermadec arc, southwest Pacific, *J. Volcanol. Geotherm. Res.*, *124*, 173–194, doi:10.1016/S0377-0273(03)00040-4.

Smith, I. E. M., T. J. Worthington, R. B. Stewart, R. C. Price, and J. A. Gamble (2003b), Felsic volcanism in the Kermadec arc, SW Pacific: Crustal recycling in an oceanic setting, in *Intra-Oceanic Subduction Systems: Tectonic and Magmatic Processes*, edited by R. D. Larter and P. T. Leat, *Geol. Soc. London Spec. Publ.*, *219*, 99–118.

Smith, I. E. M., T. J. Worthington, R. C. Price, R. B. Stewart, and R. Maas (2006), Petrogenesis of dacite in an oceanic subduction environment: Raoul Island, Kermadec arc, *J. Volcanol. Geotherm. Res.*, *156*, 252–265, doi:10.1016/j.jvolgeores.2006.03.003.

Stoffers, P., et al. (2006), Submarine volcanoes and high-temperature hydrothermal venting on the Tonga arc, southwest Pacific, *Geology*, *34*, 453–456, doi:10.1130/G22227.1.

Swanson, S. E., M. T. Naney, and H. R. Westrich (1989), Crystallisation history of Obsidian Dome, Inyo Domes, California, *Bull. Volcanol.*, *51*, 161–176, doi:10.1007/BF01067953.

Tamura, Y., and Y. Tatsumi (2002), Remelting of an andesitic crust as a possible origin for rhyolitic magma in oceanic arcs: An example from the Izu-Bonin arc, *J. Petrol.*, *43*, 1029–1047, doi:10.1093/petrology/43.6.1029.

Taylor, B., A. Klaus, G. R. Brown, G. F. Moore, Y. Okamura, and F. Murakami (1991), Structural development of the Sumisu rift, Izu-Bonin Arc, *J. Geophys. Res.*, *96*, 16,113–16,129, doi:10.1029/91JB01900.

Tsuchiyama, A. (1985), Dissolution kinetics of plagioclase in the melt of the system diopside-albite-anorthite, and the origin of dusty plagioclase in andesite, *Contrib. Mineral. Petrol.*, *89*, 1–16, doi:10.1007/BF01177585.

Watanabe, T., T. Koyaguchi, and T. Seno (1999), Tectonic stress controls on the ascent and emplacement of magmas, *J. Volcanol. Geotherm. Res.*, *91*, 65–78, doi:10.1016/S0377-0273(99)00054-2.

Worthington, T. J., M. R. Gregory, and V. Bondarenko (1999), The Denham caldera on Raoul Volcano: Dacitic volcanism in the Tonga-Kermadec arc, *J. Volcanol. Geotherm. Res.*, *90*, 29–48, doi:10.1016/S0377-0273(99)00018-9.

Wright, I. C. (1994), Nature and tectonic setting of the southern Kermadec submarine arc volcanoes: An overview, *Mar. Geol.*, *118*, 217–236, doi:10.1016/0025-3227(94)90085-X.

Wright, I. C. (1996), Volcaniclastic processes on modern submarine arc stratovolcanoes: Sidescan and photographic evidence from the Rumble IV and V volcanoes, Southern Kermadec arc (SW Pacific), *Mar. Geol.*, *136*, 21–39, doi:10.1016/S0025-3227(96)00054-0.

Wright, I. C. (1997), Morphology and evolution of the remnant Colville and active Kermadec arc ridges south of 33°30′S, *Mar. Geophys. Res.*, *19*, 177–193, doi:10.1023/A:1004266932113.

Wright, I. C. (2001), In situ modification of modern submarine hyaloclastic/pyroclastic deposits by oceanic currents: And example from the Southern Kermadec arc (SW Pacific), *Mar. Geol.*, *172*, 287–307, doi:10.1016/S0025-3227(00)00131-6.

Wright, I. C., and J. A. Gamble (1999), Southern Kermadec submarine arc caldera volcanoes (SW Pacific): Caldera formation by effusive and pyroclastic eruption, *Mar. Geol.*, *161*, 207–227, doi:10.1016/S0025-3227(99)00040-7.

Wright, I. C., L. M. Parson, and J. A. Gamble (1996), Evolution and interaction of migrating cross-arc volcanism and backarc rifting: An example from the southern Havre trough (35°20′–37°S), *J. Geophys. Res.*, *101*, 22,071–22,086, doi:10.1029/96JB01761.

Wright, I. C., C. E. J. de Ronde, K. Faure, and J. A. Gamble (1998), Discovery of hydrothermal sulfide mineralisation from southern Kermadec arc volcanoes (SW Pacific), *Earth Planet. Sci. Lett.*, *164*, 335–343, doi:10.1016/S0012-821X(98)00225-8.

Wright, I. C., P. Stoffers, M. Hannington, C. E. J. de Ronde, P. Herzig, I. E. M. Smith, and P. R. L. Browne (2002), Towed-camera investigations of shallow-intermediate water-depth submarine stratovolcanoes of the southern Kermadec arc, *Mar. Geol.*, *185*, 207–218, doi:10.1016/S0025-3227(01)00285-7.

Wright, I. C., J. A. Gamble, and P. A. Shane (2003), Submarine, silicic volcanism of the Healey caldera, southern Kermadec arc (SW Pacific): Volcanology and eruption mechanisms I. Volcanology and eruption mechanisms, *Bull. Volcanol.*, *65*, 15–29.

Wright, I. C., T. J. Worthington, and J. A. Gamble (2006), New multibeam mapping and geochemistry of the 30°–35°S sector, and overview, of southern Kermadec arc volcanism, *J. Volcanol. Geotherm. Res.*, *149*, 263–296, doi:10.1016/j.jvolgeores.2005.03.021.

Wright, I. C., W. W. Chadwick Jr., C. E. J. de Ronde, D. Reymond, O. Hyvernaud, H.-H. Gennerich, P. Stoffers, K. Mackay, M. A. Dunkin, and S. Bannister (2008), Collapse and reconstruction of Monowai submarine volcano, Kermadec arc, 1998–2004, *J. Geophys. Res.*, *113*, B08S03, doi:10.1029/2007JB005138.

Yuasa, M., F. Murakami, E. Saito, and K. Watanabe (1991), Submarine topography of seamounts on the volcanic front of the Izu-Ogasawara (Bonin) arc, *Bull. Geol. Surv. Jpn.*, *42*, 703–743.

R. J. Arculus, Department of Geology, Australian National University, Canberra, ACT 0200, Australia.

I. J. Graham and A. G. Reyes, GNS Science, Lower Hutt 5010, New Zealand. (i.graham@gns.cri.nz)

K. M. Peckett and I. E. M. Smith, School of Geography, Geology and Environmental Science, University of Auckland, Auckland 1142, New Zealand.

I. C. Wright, National Institute of Water and Atmospheric Research, Wellington 6021, New Zealand.